1 **Brain-specific Drp1 Regulates Postsynaptic Endocytosis and Dendrite Formation Independently**

2 **of Mitochondrial Division**

3

4 Kie Itoh[1], Daisuke Murata[1], Takashi Kato[1], Tatsuya Yamada[1], Yoichi Araki[2], Atsushi Saito[3],

5 Yoshihiro Adachi[1], Atsushi Igarashi[1], Shuo Li[1], Mikhail V. Pletnikov[3], Richard L. Huganir[2], Shigeki

6 Watanabe[1,2], Atsushi Kamiya[3], Miho Iijima[1,*], and Hiromi Sesaki[1,*]

7

8 [1]Department of Cell Biology, [2] Solomon H. Snyder Department of Neuroscience, [3]Department of

9 Psychiatry and Behavioral Sciences, Johns Hopkins University School of Medicine, Baltimore, MD,

10 USA

11 *Corresponding authors

12

13 Running Title: Role of Drp1 in postsynaptic endocytosis
14
15
16

17

Abstract

Dynamin-related protein 1 (Drp1) divides mitochondria as a mechano-chemical GTPase. However, the function of Drp1 beyond mitochondrial division is largely unknown. Multiple Drp1 isoforms are produced through mRNA splicing. One such isoform, Drp1$_{ABCD}$, contains all four alternative exons and is specifically expressed in the brain. Here, we studied the function of Drp1$_{ABCD}$ in mouse neurons in both culture and animal systems using isoform-specific knockdown by shRNA and isoform-specific knockout by CRISPR/Cas9. We found that the expression of Drp1$_{ABCD}$ is induced during postnatal brain development. Drp1$_{ABCD}$ is enriched in dendritic spines and regulates postsynaptic clathrin-mediated endocytosis by positioning the endocytic zone at the postsynaptic density, independently of mitochondrial division. Drp1$_{ABCD}$ loss promotes the formation of ectopic dendrites in neurons and enhanced sensorimotor gating behavior in mice. These data reveal that Drp1$_{ABCD}$ controls postsynaptic endocytosis, neuronal morphology and brain function.

31

32

33

34

Introduction

The major function of Drp1, which is encoded by the *Dnm1l* gene, is to control mitochondrial division as a mechano-chemical GTPase (Kameoka et al., 2018; Kraus and Ryan, 2017; Pernas and Scorrano, 2016; Prudent and McBride, 2017; Ramachandran, 2018; Tamura et al., 2011; van der Bliek et al., 2013). During mitochondrial division, Drp1 is assembled into helical filaments around the surface of mitochondria. Through GTP hydrolysis and interactions with receptors, the Drp1 filaments change their conformation and constrict the mitochondrial membrane. Mitochondrial division is important for human health: hyper- or hypo-division caused by the mis-regulation of Drp1 has been linked to many neurological disorders, such as Alzheimer's, Parkinson's, and Huntington's diseases (Cho et al., 2010; Itoh et al., 2013; Kandimalla and Reddy, 2016; Roy et al., 2015; Serasinghe and Chipuk, 2017). Notably, human Drp1 mutations also lead to neurodevelopmental defects with post-neonatal lethality, developmental delay, late-onset neurological decline, or optic atrophy (Fahrner et al., 2016; Gerber et al., 2017; Vanstone et al., 2015; Waterham et al., 2007); however, our current understanding of Drp1's function outside of mitochondrial division is limited.

To study the function of Drp1, complete and tissue-specific knockout (KO) mice for Drp1 have been characterized. The loss of Drp1 results in mitochondrial elongation and enlargement due to unopposed mitochondrial fusion in the absence of mitochondrial division in many cells (Friedman and Nunnari, 2014; Kashatus, 2018; Widlansky and Hill, 2018; Youle and van der Bliek, 2012). Complete loss causes embryonic lethality (Ishihara et al., 2009; Wakabayashi et al., 2009), whereas neuron-specific KO leads to a wide range of phenotypes, depending on the types of neurons and the timings when Drp1 is knocked out. For example, the loss of Drp1 in cerebellar

57 Purkinje cells results in developmental defects when knocked out in embryos and progressive

58 degeneration when knocked out in post-mitotic adult Purkinje cells (Kageyama et al., 2012;

59 Wakabayashi et al., 2009). Similar to Purkinje cells, the loss of Drp1 induces massive death in

60 dopaminergic neurons (Berthet et al., 2014). In contrast, hippocampal neurons are more

61 resistant to the loss of Drp1; hippocampal neurons that lack Drp1 or express dominant negative

62 Drp1, do not die but instead show deficits in bioenergetic and synaptic functions (Divakaruni et

63 al., 2018; Shields et al., 2015). Similarly, Drp1-KO hypothalamic pro-opiomelanocortin neurons

64 are also viable and show increased glucose and leptin sensing (Santoro et al., 2017).

65   Drp1 is encoded by a single gene and produces multiple isoforms through alternative

66 splicing of mRNAs. There are four alternative exons in Drp1 in mice (termed A, B, C, and D)

67 (Figure 1A). These alternative exons are located in either the GTPase domain (A and B) or the

68 variable domain (C and D), which is mainly intrinsically disordered and contains regulatory

69 phosphorylation sites (Itoh et al., 2018). All of the Drp1 isoforms are located at mitochondria and

70 function in mitochondrial division (Itoh et al., 2018). Interestingly, a subset of these isoforms is

71 also located at additional sites. For example, $Drp1_D$ and $Drp1_{BD}$ are associated with and regulate

72 the dynamics of microtubules (Itoh et al., 2018; Strack et al., 2013). We recently identified a

73 novel isoform of Drp1 (termed $Drp1_{ABCD}$) that is exclusively expressed in the brain (Itoh et al.,

74 2018). $Drp1_{ABCD}$, which contains all of the alternative exons, is the only isoform that is associated

75 with lysosomes, late endosomes, and the plasma membrane when this isoform is expressed in

76 Drp1-KO mouse embryonic fibroblasts (MEFs) (Itoh et al., 2018). Analysis of transcripts and

77 proteins showed that $Drp1_{ABCD}$ is expressed at low levels; $Drp1_{ABCD}$ constitutes less than 5% of all

78 the Drp1 isoforms expressed in the brain (Itoh et al., 2018).

79   The unique localization of Drp1$_{ABCD}$ suggests that this brain-specific isoform may play a

80   role in membrane trafficking in neurons; however, its function remains to be determined

81   because of the lack of tools to specifically assess its function without affecting other isoforms. In

82   this study, we have developed isoform-specific knockdown by shRNA and knockout by

83   CRISPR/Cas9. Using these new approaches, we found that Drp1$_{ABCD}$ controls postsynaptic

84   endocytosis and dendrite growth in neurons independently of mitochondrial division.

85

86   **Results and Discussion**

87   **Drp1$_{ABCD}$ expression is induced during postnatal brain development**

88   Since Drp1$_{ABCD}$ is the only isoform that contains both the alternative exons A and B (Figure

89   1A), we raised antibodies that specifically recognize Drp1$_{ABCD}$ using the amino acid sequence that

90   corresponds to the junction of exons A and B as an antigen (Itoh et al., 2018). The expression of

91   Drp1$_{ABCD}$ was spatially controlled and specific to the brain (Itoh et al., 2018) (Figure 1B). In the

92   brain, Drp1$_{ABCD}$ was ubiquitously expressed in multiple subregions, including the hippocampus,

93   cortex, midbrain, striatum, and cerebellum (Itoh et al., 2018).

94   To test whether the expression of Drp1$_{ABCD}$ is temporarily regulated in the brain, we

95   performed Immunoblotting of whole brain and hippocampus tissues that were harvested from

96   mice at the ages of P0, P8, 1 month, and 2 months. We found that the expression of Drp1$_{ABCD}$ is

97   postnatally induced in both tissues later in neural development compared to that of postsynaptic

98   density protein 95 (Psd-95), which is a synaptic protein required for glutamate receptor

99   organization (Figure 1C). In contrast, anti-pan-Drp1 antibodies, which recognize all Drp1

100   isoforms, showed similar levels of Drp1 at different stages of postnatal brain development

101   (Figure 1C). Consistent with the *in vivo* data, immunoblotting of hippocampal neurons cultured *in*

102   *vitro* showed that the expression of Drp1$_{ABCD}$ gradually increases and reaches a plateau around 3

103   weeks (Figure 1D).

104

105   **Drp1$_{ABCD}$ is enriched in postsynaptic terminals**

106   To examine the subcellular localization of Drp1$_{ABCD}$ in neurons, we expressed HA-Drp1$_{ABCD}$

107   along with a cytosolic marker, tdTomato, in cultured hippocampal neurons. For a comparison, we

108   tested HA-Drp1$_{BCD}$, the most abundant brain Drp1 isoform (Itoh et al., 2018). In the soma, both

109   HA-Drp1$_{ABCD}$ and HA-Drp1$_{BCD}$ appeared to be uniformly distributed (Figure 1E). We did not

110   observe a clear association between these HA-tagged Drp1 isoforms and mitochondria,

111   lysosomes, or the plasma membrane, likely due to their overexpression and therefore high levels

112   in the cytoplasm. Interestingly, however, we found that HA-Drp1$_{ABCD}$ is enriched in postsynaptic

113   regions, compared to HA-Drp1$_{BCD}$ (Figure 1E). Line scanning analysis of their fluorescence showed

114   a significant increase in the signal ratio of HA-Drp1$_{ABCD}$ (spine vs dendritic shaft), compared to

115   HA-Drp1$_{BCD}$ (Figure 1F and G). Analysis of HA-Drp1$_{ABCD}$ and HA-Drp1$_{BCD}$ in synapses at high

116   magnification suggested its preferential localization of HA-Drp1$_{ABCD}$ around the postsynaptic

117   density, which is in a close apposition to the pre-synaptic marker vesicular glutamate transporter

118   1 (Figure 1H).

119   To test the localization of endogenous Drp1$_{ABCD}$ at the postsynaptic density, we

120   biochemically obtained postsynaptic density fractions from the brains of mice (Araki et al., 2015)

121   since anti-Drp1$_{ABCD}$ antibodies do not work in immunofluorescence of the endogenous protein.

122   Consistent with the immunofluorescence data, increased levels of Drp1$_{ABCD}$ were co-fractionated

123   with the postsynaptic density, compared to total Drp1 detected by pan-Drp1 antibodies (Figure

124   1I and J).

125

126   **The loss of Drp1$_{ABCD}$ inhibits endocytosis at postsynaptic terminals**

127   To examine the function of Drp1$_{ABCD}$ at the postsynaptic density, we homozygously

128   deleted exon A using the CRISPR/Cas9 genome editing system (termed Drp1$_{exonA}$-KO mice) since

129   Drp1$_{ABCD}$ is the only isoform that contains this exon (Itoh et al., 2018) (Figure 2A). We confirmed

130   the lack of Drp1$_{ABCD}$ proteins in Drp1$_{exonA}$-KO mice using Immunoblotting (Figure 2B). Consistent

131   with a low expression level of Drp1$_{ABCD}$ (compared to that of other isoforms, such as Drp1$_{BCD}$)

132   (Itoh et al., 2018), we found no gross changes in the total amount of Drp1 in Immunoblotting

133   using anti-pan-Drp1 antibodies (Figure 2B). Drp1$_{exonA}$-KO mice were born at an expected

134   Mendelian ratio with normal weights of the body and brain (Figure 2C-E). H&E staining of sagittal

135   brain sections showed that the histology of the cerebellum appears to be normal in Drp1$_{exonA}$-KO

136   mice (Figure 2F). DAPI staining also showed similar nuclear patterns of neurons and the thickness

137   of the CA1 layer in the hippocampus in control and Drp1$_{exonA}$-KO mice (Figure 2G). These data

138   suggest that the loss of Drp1$_{ABCD}$ does not change the overall structure of the brain.

139   We isolated hippocampal neurons from E18.5 mouse embryos and cultured them *in vitro*

140   for 3 weeks. We then examined synapses by transmission electron microscopy. In both control

141   and Drp1$_{exonA}$-KO neurons, we observed matured synaptic contacts (Figure 2H). However,

142   remarkably, the number of clathrin-coated pits (CCPs) was significantly different in these

143   neurons—Drp1$_{exonA}$-KO neurons showed more CCPs in postsynaptic terminals compared with

144   control neurons (Figure 2H and I). In contrast, the number of CCPs in presynaptic terminals was

145   indistinguishable (Figure 2H and J). We then divided the morphologies of CCPs in postsynaptic

146   terminals into three categories: shallow, U-shaped and omega-shaped pits. We found an

147   increased frequency of shallow and U-shaped CCPs, which likely represent early stages during

148   endocytosis, in Drp1$_{exonA}$-KO neurons (Figure 2K and L). The frequencies of omega-shaped CCPs

149   were similar in control and Drp1$_{exonA}$-KO neurons (Figure 2K and L).

150   The observed increase in the number of CCPs could be explained by either activation or

151   inhibition of endocytosis. First, the rate of clathrin-mediated endocytosis may be enhanced in

152   Drp1$_{exonA}$-KO neurons and therefore shallow and U-shaped CCPs were observed at a higher

153   frequency. Alternatively, clathrin-mediated endocytosis may be slowed at early stages after the

154   initiation of endocytosis perhaps in Drp1$_{exonA}$-KO neurons and thereby the intermediates were

155   accumulated. To distinguish between these two possibilities, we treated control and Drp1$_{exonA}$-

156   KO neurons with dynasore, a dynamin inhibitor that blocks the final step of endocytosis (Macia et

157   al., 2006), for 30 min prior to chemical fixation for electron microscopy. As expected, dynasore

158   significantly increased the number of CCPs at postsynaptic terminals in control neurons (Figure

159   2M and N). In contrast, when we treated Drp1$_{exonA}$-KO neurons with dynasore, we found no

160   increase in the number of CCPs (Figure 2M and N). Thus, it is likely that the rate of clathrin-

161   mediated endocytosis is decreased in Drp1$_{exonA}$-KO neurons. The accumulation of shallow and U-

162   shaped CCPs, but not omega-shaped ones, suggest that Drp1$_{ABCD}$ may function at an early step

163   upstream of the constriction and severing of the neck of coated pits that is mediated by dynamin

164   (Figure 2S). We confirmed that dynasore did not inhibit Drp1 by examining mitochondrial

165   morphology in neurons and mouse embryonic fibroblasts using electron microscopy and

166   immunofluorescence microscopy with antibodies to a mitochondrial protein (pyruvate

167   dehydrogenase, PDH), we confirmed that (Figure 2O, 2P; Figure 2—figure supplement 1).

168   To further examine the consequence of $Drp1_{ABCD}$ loss in clathrin-mediated endocytosis,

169   we stimulated WT and KO neurons with N-methyl-D-aspartic acid (NMDA) for a short period of

170   time (3 min) and analyzed the number of CCPs at the postsypatic terminal. When we stimulated

171   neurons in the presence of dynasore, the number of postsynaptic clathrin-coated pits increased

172   in control neurons. This is due to stimulation of endocytosis by NMDA and inhibition of its

173   completion by dynasore. In contrast, the number of CCPs remained unchanged in $Drp1_{exonA}$-KO

174   neurons (Figure 2Q). These phenotypes of $Drp1_{ABCD}$ loss were only observed at the postsynaptic

175   region and not the presynaptic region (Figure 2R). These data further support the notion that

176   postsynaptic clathrin-mediated endocytosis is slow in $Drp1_{exonA}$-KO neurons even when

177   stimulated by NMDA (Figure 2S). Interestingly, when stimulated by NMDA in the absence of

178   dynasore, the number of CCPs was decreased in $Drp1_{exonA}$-KO neurons (Figure 2Q). It appears

179   that NMDA induces internalization of some endocytic vesicles in $Drp1_{exonA}$-KO neurons. We

180   suggest that $Drp1_{exonA}$-KO neurons have slow kinetics of endocytosis but do not completely block

181   it (Figure 2S).

182   To understand how $Drp1_{ABCD}$ loss results in changes in CCPs, we tested postsynaptic

183   positioning of the endocytic zone using mCherry-clathrin light chain (mCherry-CLC) and Psd-95-

184   Fibronectin intrabodies (Gross et al., 2013; Lu et al., 2007). As previously reported (Lu et al.,

185   2007), the majority of mCherry-CLC signals are localized next to Psd-95 signals in control neurons

186   (Figure 3A and B). In contrast, we found a higher frequency of dissociation of mCherry-CLC

187   signals from Psd-95 signals in $Drp1_{exonA}$-KO neurons (Figure 3A and B). We speculate that

188   decreased levels of clathrin in the synapses in Drp1$_{exonA}$-KO neurons slow the progression of

189   endocytosis. In these synapses, the formation of CCPs is initiated; however, the maturation of

190   CCPs is likely decreased due to the limited availability of clathrin molecules. As a result, CCPs

191   accumulate during relatively early stages of endocytosis (e.g., shallow and U-shaped CCPs)

192   (Figure 2L). These data suggest that Drp1$_{ABCD}$, unlike dynamin, does not play a role in the scission

193   of the neck of coated pits.

194   The extent of the dissociation of the postsynaptic density from the endocytic zone in

195   Drp1$_{exonA}$-KO synapses is similar to that reported for the disruption of Homer, an adaptor protein

196   that connects the postsynaptic density and endocytic zone (Lu et al., 2007). Like Homer defective

197   neurons, the uptake of FITC-transferrin was not affected in Drp1$_{exonA}$-KO neurons (Figure 3—

198   figure supplement 1). In contrast to the Homer pathway, however, we found that AMPA

199   receptors, such as GluR1, GluR2 and GluR3, are normally expressed on the plasma membrane of

200   Drp1$_{exonA}$-KO neurons in surface biotinylation experiments (Figure 3C and D). Furthermore,

201   endocytosis of GFP-GluR1 in response to NMDA stimulation was not perturbed in Drp1$_{exonA}$-KO

202   neurons (Figure 3E and F). These data suggest that the Drp1$_{ABCD}$ pathway has cargos that differ

203   from those of the Homer pathway (Figure 3G).

204   Using immunofluorescence microscopy, we observed no gross changes in the morphology

205   of mitochondria in proximal and distal regions along with dendrites in Drp1$_{exonA}$-KO neurons

206   (Figure 3H-J). Therefore, inhibition of endocytosis does not appear to be the result of defects in

207   mitochondrial morphology. It is likely that other Drp1 isoforms, such as Drp1$_{BCD}$ and Drp1$_{CD}$,

208   which together constitute the majority of Drp1 isoforms in the brain (Itoh et al., 2018), mainly

209   control mitochondrial division and morphology.

210   A previous study reported that Drp1 regulates endocytosis for synaptic vesicle recycling at

211   presynaptic terminals in hippocampal neurons through interactions with a Drp1 receptor protein,

212   Mff (Li et al., 2013). Since we found endocytic defects only at postsynaptic terminals in Drp1$_{exonA}$-

213   KO neurons, distinct Drp1 isoforms may function separately in endocytosis at pre- and

214   postsynaptic terminals.

215

216   **The loss of Drp1$_{ABCD}$ induces the extension of ectopic dendrites in cultured neurons**

217   Intriguingly, during analysis of the morphology of cultured hippocampal neurons, we

218   noticed that Drp1$_{exonA}$-KO neurons significantly increased the number of primary dendrites with

219   dendritic spines (e.g., dendrites that directly emerged from the soma), compared to control

220   neurons (Figure 4A and B). The number of axons that lack spines remained unchanged (one axon

221   per neuron). The effect of Drp1$_{ABCD}$ loss was specific to the number of primary dendrites. We

222   observed no significant difference in the number of dendritic branches between control and

223   Drp1$_{exonA}$-KO neurons (Figure 4C) or the density of dendritic spines (Figure 4D).

224   To further test whether Drp1$_{ABCD}$ controls dendrite formation in neurons in a cell-

225   autonomous fashion, we specifically knocked down Drp1$_{ABCD}$ in cultured hippocampal neurons

226   using shRNAs. To target Drp1$_{ABCD}$, we used an mRNA sequence that corresponds to the junction

227   between exon A and exon B, which is unique to Drp1$_{ABCD}$ (Figure 4E). First, the specificity of this

228   knockdown construct was confirmed. We individually expressed each of GFP-Drp1$_{ACD}$, GFP-

229   Drp1$_{BCD}$, and GFP-Drp1$_{ABCD}$ in separate HEK293 cells. We found that AB-targeted shRNA

230   specifically knocked down GFP-Drp1$_{ABCD}$, but not GFP-Drp1$_{ACD}$ or GFP-Drp1$_{BCD}$ (Figure 4F, AB

231   shRNA). As a negative control, scramble shRNA was used (Figure 4F, Scramble). As a positive

232 control, we targeted an mRNA sequence that is common in all Drp1 isoforms (Figure 4F, Pan-

233 Drp1).

234   Supporting the data from the above experiments using Drp1$_{exonA}$-KO neurons, AB-

235 targeted shRNA significantly increased the number of primary dendrites in cultured neurons at

236 both 2 and 3 weeks compared to scramble shRNA (Figure 4G and H). Ectopic dendrites extended

237 within a short period of time (3 days) after knockdown of Drp1$_{ABCD}$ in mature neurons with

238 developed dendrites. The number of axons did not change (one axon per neuron) as assessed by

239 immunofluorescence microscopy with anti-MAP2 antibodies, which label dendrites but not axons

240 (Figure 4—figure supplement 1). To confirm that the induction of dendrite formation results

241 from the knockdown of Drp1$_{ABCD}$, we co-expressed plasmids carrying a knockdown-resistant form

242 of Drp1$_{ABCD}$ along with AB-targeted shRNAs. The Drp1$_{ABCD}$ plasmid, but not the empty plasmid,

243 significantly rescued the effect of AB-targeted shRNAs (Figure 4I). These data further support the

244 notion that Drp1$_{ABCD}$ is important for controlling the number of primary dendrites in neurons.

245   Dendrite growth is regulated by neuronal activity-dependent and -independent

246 mechanisms (Wong and Ghosh, 2002). To understand the mechanism underlying the ectopic

247 dendrite formation in AB-targeted neurons, we treated hippocampal neurons during knockdown

248 with tetrodotoxin, a sodium channel inhibitor that blocks action potentials. We found that

249 tetrodotoxin significantly blocked the effect of Drp1$_{ABCD}$ knockdown on ectopic dendrite

250 formation, but did not affect the number of dendrites in control neurons (Figure 4J). These data

251 suggest that the formation of primary dendrites induced by Drp1$_{ABCD}$ depletion requires neuronal

252 activity.

253

Loss of Drp1$_{ABCD}$ induces the formation of ectopic primary dendrites *in vivo*

To test the function of Drp1$_{ABCD}$ in the morphology of neurons *in vivo*, we analyzed the morphology of neurons in Drp1$_{exonA}$-KO mice. To achieve this goal, it was critical to sparsely label individual neurons because the density of neurons is too high to faithfully visualize the morphology of each neuron if all of the neurons are labeled. We crossed Drp1$_{exonA}$-KO mice with a mouse line that expresses a cytosolic GFP in a small number of neurons driven by the neuron-specific Thy1 promoter (Feng et al., 2000) (Figure 4—figure supplement 2). We counted the number of neurites using z stacks of laser confocal microscopy of frozen brain sections. We found a significant increase in the number of neurites in the CA1 and CA2 layers in the dorsal hippocampus (Figure 4K) consistent with the data from the *in vitro* experiments. The effect of Drp1$_{ABCD}$ loss on primary dendrites was also evident in the cortex (Figure 4L).

To further test the effect of Drp1$_{ABCD}$ knockdown during brain development *in vivo*, we performed *in utero* electroporation of shRNAs. We injected plasmids carrying scramble or AB-targeted shRNA, along with plasmids carrying cytosolic GFP, into the lateral ventricles of E15.5 embryos in timed pregnant mice using a glass micropipette (Figure 4M). We then performed electroporation to introduce the plasmids into the hippocampus, after which the embryos were returned to the abdomen. At 7 weeks after birth, mice were fixed using cardiac perfusion of paraformaldehyde (Figure 4M). Coronal cryosections of the CA1 and 2 layers in the dorsal hippocampus were cut and the neuronal morphology was analyzed using z stacks of laser confocal microscopy images. Since the cytosolic GFP labels both dendrites and axons, we counted the number of neurites (including both dendrites and axons) that directly emerged from the soma. Consistent with the knockout results, we found that knockdown of Drp1$_{ABCD}$

276   significantly increased the number of neurites, compared to the scramble control, in the

277   hippocampus *in vivo* (Figure 4N).

278

279   **The loss of Drp1$_{ABCD}$ increases sensorimotor gating function**

280   To test whether the loss of Drp1$_{ABCD}$ affects brain function, behavioral phenotypes were

281   systematically characterized in control and Drp1$_{exonA}$-KO mice. We observed normal general

282   locomotor activities in Drp1$_{exonA}$-KO mice in open field test (Figure 4—figure supplement 3A).

283   Intriguingly, KO mice exhibited significantly increased prepulse inhibition (PPI) of the acoustic

284   startle without alterations in the startle response (Figure 4O and P). PPI, as a measure of

285   sensorimotor gating, involves several brain regions (including the hippocampus, medial

286   prefrontal cortex, amygdala, and nucleus accumbens) (Lee and Davis, 1997; Swerdlow et al.,

287   2001). Sensorimotor gating function enables selective attention that distinguishes or separates

288   critical information from background noise. In humans, sensorimotor gating function is often

289   referred to as the cocktail party effect, which allows one to talk with someone even in a crowded

290   party environment (Lee and Davis, 1997; Swerdlow et al., 2001). This gating function is important

291   for human health and its defects have been associated with mental illness, such as schizophrenia

292   and autism spectrum disorders (Lee and Davis, 1997; Swerdlow et al., 2001). At this moment, we

293   do not know the exact mechanistic basis underlying this enhanced sensorimotor gating in

294   Drp1$_{exonA}$-KO mice; however, the increased number of dendrites or the decreased postsynaptic

295   endocytosis in Drp1$_{exonA}$-KO mice may contribute to the enhancement in sensorimotor gating

296   function. Behavioral changes in Drp1$_{exonA}$-KO mice appeared to be specific to sensorimotor gating

297   since we observed no alterations in spatial working and recognition memory tasks in Y-maze

298 tests (Figure 4—figure supplement 3B), motor coordination in rotarod test (Figure 4—figure

299 supplement 3C), and anxiety level in elevated plus maze test (Figure 4—figure supplement 3D).

300 In summary, we found, for the first time, that the novel brain-specific isoform $Drp1_{ABCD}$

301 controls postsynaptic endocytosis independently of mitochondrial division. It would be important

302 to test if this, in turn, results in the accumulation of cargoes on the postsynaptic surface and

303 leads to ectopic formation of dendrites in future studies. Since the expression of $Drp1_{ABCD}$ is

304 induced during the postnatal period, $Drp1_{ABCD}$ may control the number of dendrites by

305 suppressing unwanted, excess dendrite formation in neuronal network wiring during postnatal

306 brain development.

307

308 **Methods**

309 **Key resources table**

Reagent type (species) or resource	Designation	Source or reference	Identifiers	Additional information
genetic reagent (*M. musculus*)	Wild-type mice	This paper		Materials and methods: Generation of $Drp1_{exonA}$-KO mice using CRISPR/Cas9
genetic reagent (*M. musculus*)	$Drp1_{exonA}$-KO mice	This paper		Materials and methods: Generation of $Drp1_{exonA}$-KO mice using CRISPR/Cas9
genetic reagent (*M. musculus*)	Thy1-GFP-M transgenic mice	Jackson Laboratory	Stock #: 007788	
genetic reagent (*M. musculus*)	C57BL/6J mice	Jackson Laboratory	Stock #: 000664	

cell line ()	WT and Drp1-KO MEFs	Kageyama et al., 2014		
antibody	Rabbit polyclonal anti-exon AB	Itoh et al., 2018		WB (1:2000)
antibody	Mouse monoclonal anti-Psd-95	EMD Millipore	Cat #: MABN68	WB (1:2000)
antibody	Mouse monoclonal anti-pan-Drp1	BD Biosciences	Cat #: 611113	WB (1:2000)
antibody	Mouse monoclonal anti-PDH subunit E2/E3bp	Abcam	Cat #: ab110333	IF (1:300)
recombinant DNA reagent	HA-Drp1$_{ABCD}$	Itoh et al., 2018		
recombinant DNA reagent	HA-Drp1$_{BCD}$	Itoh et al., 2018		
recombinant DNA reagent	Psd95.FingR-GFP	Addgene	Cat #: 46295	Gross et al., 2013
recombinant DNA reagent	mCherry-Clathrin (CLC)	Addgene	Cat #: 27680	
recombinant DNA reagent	Psd-95-mCherry	Blanpied et al., 2008		
recombinant DNA reagent	GFP-GluR1	Hussain et al., 2015		
recombinant DNA reagent	pSUPER-Scramble	This paper		Materials and methods: Plasmids
recombinant DNA reagent	pSUPER-AB	This paper		Materials and methods: Plasmids
recombinant DNA reagent	pSUPER-GFP-Scramble	This paper		Materials and methods: Plasmids
recombinant DNA reagent	pSUPER-GFP-AB	This paper		Materials and methods: Plasmids
recombinant DNA reagent	pCAGGS1-Drp1$_{ABCD}$ (resistant form)	This paper		Materials and methods: Plasmids
chemical compound, drug	Dynasore hydrate	Sigma-Aldrich	Cat #: D7693	
chemical	NMDA	Tocris	Cat #: 0114	

chemical compound, drug				
chemical compound, drug	Glycine	Tocris	Cat #: 0219	
chemical compound, drug	Tetrodotoxin (TTX)	Tocris	Cat #: 1078	

310

311 **Generation of Drp1$_{exonA}$-KO mice using CRISPR/Cas9**

312   All animal work was conducted according to the guidelines established by the Johns

313 Hopkins University Committee on Animal Care and Use. To engineer the mouse Dnm1l gene that

314 encodes Drp1, sgRNA-encoding sequences (5'- AAAATGGTAAATTTCAGAGC- 3' to target inside the

315 A exon and 5'-TAAAAAGTTGATTGGTGAAT- 3' to target downstream of the A exon) were cloned

316 into the BbsI site of pX330-T7 and amplified from pX330-T7 with a leading T7 promoter by PCR

317 (Igarashi et al., 2018). These sgRNAs were *in vitro* transcribed using the HiScribe T7 Quick High

318 Yield RNA Synthesis Kit (New England Biolabs) and purified using the MEGAclear Kit (Ambion).

319 Cas9 mRNA was *in vitro* transcribed using NotI-linearized pX330-T7 and the mMESSAGE

320 mMACHINE T7 Ultra Kit (Ambion) and purified by LiCl precipitation. Pronuclear injections of

321 zygotes from B6SJLF1/J mice (Jackson Laboratory, stock no. 100012) were performed at the

322 Johns Hopkins University Transgenic Facility using a mix of Cas9 mRNA and two sgRNA-encoding

323 sequences in injection buffer (10 mM Tris-HCl, 0.1 mM EDTA filtered with 0.2-μm pore size).

324 Three combinations of concentrations were used: 100 ng/μl of Cas9 mRNA and 50 ng/μl of each

325 sgRNA, 100 ng/μl Cas9 of mRNA and 25 ng/μl of each sgRNA, and 25 ng/μl of Cas9 mRNA and

326 12.5 ng/μl of each sgRNA. The embryos were cultured at 37 °C in the CO_2 incubator for 2 h and

327 then transferred into the oviducts of pseudopregnant ICR females (25 embryos per mouse)

328   (Envigo). Sixteen pups were obtained and their genotypes were analyzed by PCR using the

329   following primers: 5'-AGACCTCTCATTCTGCAGCT-3' and 5'-GTGGATGGTCGCTGAGTTTG-3'. We

330   identified one founder mouse that truncated 96 bp to remove the A exon, resulting in A knock

331   out. The A exon (KFQSWN) was replaced with 20 amino acids (KWEIIAIAKSEIFRIGINI) and a stop

332   codon. By breeding with the Thy1-GFP-M transgenic mouse line (Jackson Laboratory, stock no.

333   007788), we generated Thy1-GFP/homozygous $Drp1_{exonA}$-KO mice and Thy1-GFP/wild-type mice.

334

335   **Plasmids**

336   To create the HA-$Drp1_{BCD}$ plasmid, $Drp1_{ABCD}$ in the HA-$Drp1_{ABCD}$ plasmid (Itoh et al., 2018)

337   was replaced with the full length of $Drp1_{BCD}$ at the BamHI/NotI sites. To create the GFP-$Drp1_{ABCD}$

338   plasmid, $(SAGG)_5$ linker sequence and full-length $Drp1_{ABCD}$ were cloned into the BglII/EcoRI sites

339   and the XhoI/SmaI sites of pEGFP-C1 (Clontech), respectively. $Drp1_{ABCD}$ was replaced with $Drp1_{ACD}$

340   and $Drp1_{BCD}$ to create the GFP-$Drp1_{ACD}$ and GFP-$Drp1_{BCD}$ plasmids. To generate the shRNA

341   plasmids, the following target sequences were cloned into pSUPER (Oligoengine, VEC-PBS-0002)

342   or pSUPER-GFP (Yamada et al., 2018). Scramble:

343   CCTAAGGTTAAGTCGCCCTCGttcaagagaCGAGGGCGACTTAACCTTAGG, AB:

344   ATTTCAGAGCTGGAACCCTGCttcaagagaGCAGGGTTCCAGCTCTGAAAT, and Pan-Drp1:

345   GCTTCAGATCAGAGAACTTATttcaagagaATAAGTTCTCTGATCTGAAGC. To generate a knockdown-

346   resistant $Drp1_{ABCD}$ plasmid, both target sequences for AB and pan-Drp1 were replaced to the

347   following resistant form. AB: ATTTCAGAGCTGGAACCCTGC to G<u>T</u>TC<u>C</u>A<u>A</u>AG<u>T</u>TGGAA<u>T</u>CC<u>A</u>GC, and

348   pan-Drp1: GCTTCAGATCAGAGAACTTAT to G<u>T</u>TGCA<u>A</u>AT<u>T</u>C<u>G</u>CGA<u>G</u>CT<u>G</u>AT. Underlined cases are the

349   added silent mutations. Full length of Drp1$_{ABCD}$ with silent mutations was cloned into the

350   XhoI/NotI sites of pCAGGS1 vector.

351

352   **Immunoblotting**

353   Mouse tissues were harvested, flash-frozen in liquid nitrogen, and homogenized in RIPA

354   buffer (Cell Signaling Technology, 9806) that contained cOmplete Mini Protease Inhibitor (Roche,

355   11836170001). Lysates were centrifuged at 14,000 x g for 10 min at 4°C and the supernatants

356   were collected. Proteins were separated by SDS–PAGE and transferred onto Immobilon-FL

357   membranes (Millipore). The antibodies used were exon AB (Itoh et al., 2018), Pan-Drp1 (BD

358   Biosciences, 611113), PDH subunit E2/E3bp (Abcam, ab110333), GAPDH (Thermo, MA5-15738),

359   actin (Santa Cruz Biotechnology, sc-1615), Psd-95 (EMD Millipore, MABN68), clathrin (BD

360   Biosciences, 610499), beta-III tubulin (Abcam, ab18207), GFP (Molecular probe, A11121), GluR1

361   (EMD Millipore, MAB397), GluR2 (Araki et al., 2010) and GluR3 (Araki et al., 2010).

362   Immunocomplexes were visualized using fluorescently-labeled secondary antibodies and

363   detected using a PharosFX Plus Molecular Imager (Bio-Rad).

364

365   **Neuronal cultures and immunofluorescence microscopy**

366   Hippocampal neurons were isolated and cultured *in vitro* as previously described (Araki et

367   al., 2015). In brief, E18.5 embryos were decapitated, and brains were quickly removed and

368   transferred in cold Dissection media [1 x HBSS (Gibco, 14185052), 1 mM sodium pyruvate (Gibco,

369   11360070), 10 mM HEPES (Gibco, 15630080), 30 mM glucose, 100 U/ml penicillin, and 100 µg/ml

370   streptomycin]. Hippocampi were dissected under a binocular microscope and incubated in

371   Dissection medium supplemented with 0.5 mg/ml papain (Worthington, LS003119) and 0.01%

372   DNase (Sigma, DN25) for 20 min at 37 °C. Hippocampi were washed once with warm Neurobasal

373   medium (Gibco, 21103049) supplemented with 100 U/ml penicillin, 100 µg/ml streptomycin, 2

374   mM GlutaMax (Gibco, 35050061), 2% B-27 (Gibco, 17504044) and 5% horse serum (Gibco,

375   26050088). Neurons were triturated and plated on 18-mm poly-L-lysine-coated coverslips at a

376   density of 160,000 cells/well in 12-well tissue culture plates in 1 ml of the Neurobasal medium

377   supplemented with 100 U/ml penicillin, 100 µg/ml streptomycin, 2 mM GlutaMax, 2% B-27 and

378   5% horse serum. After 24 h, neurons were switched and maintained thereafter in Neurobasal

379   media with 2 mM GlutaMax and 2% B-27. Cultured neurons were fed with half-media changes

380   once per week. Cells were transfected with Lipofectamin 2000 (Invitrogen) in accordance with

381   the manufacturer's manual. After 2-3 days, neurons were fixed using PBS containing 4%

382   paraformaldehyde, washed in PBS, permeabilized with 0.2% Triton X-100/PBS, and blocked in

383   0.5% BSA/PBS (Adachi et al., 2016). The cells were incubated with antibodies to Pan-Drp1, HA

384   (Novus Biologicals, NB600-362), RFP (antibodies-online, ABIN129578), VGLUT1 (Synaptic systems,

385   135304), MAP2 (Thermo Fisher, MA5-12826) and PDH subunit E2/E3bp, followed by the

386   appropriate secondary antibodies. Samples were mounted in Prolong Gold Antifade Reagent (Cell

387   Signaling, 9071) and viewed using Zeiss LSM510-Meta, LSM700 FCS, and LSM800 GaAsP laser

388   scanning confocal microscopes. To determine the size of the mitochondria in the dendrites, we

389   first examined serial confocal images along the Z-axis to identify individual mitochondria and

390   then measured their length using ImageJ.

391

392   **PSD fractionation**

393   Fractionation of post-synaptic density was performed as described previously (Araki et al.,

394   2015). In brief, mouse whole brain was dissected and homogenized by a dounce homogenizer 30

395   times in Buffer A (0.32 M sucrose, 10 mM Hepes, pH7.4, with cOmplete Mini Protease Inhibitor).

396   The homogenate was centrifuged at 1,000 x g for 10 min at 4 °C. The post-nuclear supernatant

397   was collected and centrifuged at 13,800 x g for 20 min at 4 °C. The supernatant was kept as S2

398   fraction. The pellet was resuspended in 3 volumes of Buffer A (P2 fraction). The P2 fraction was

399   layered onto a discontinuous sucrose gradient (0.85, 1.0, and 1.4 M) in 10 mM Hepes (pH7.4)

400   with cOmplete Mini Protease Inhibitor and centrifuged at 82,500 x g for 2 h at 4 °C. The interface

401   between 1.0 and 1.4 M sucrose was collected as the synaptosome fraction (Syn) and diluted with

402   80 mM Tris-HCl (pH 8.0). An equal volume of 1% Triton X-100 was added and rotated for 10 min

403   at 4 °C, then centrifuged at 32,000 x g for 20 min. The supernatant was collected as Triton-

404   soluble synaptosome (Syn/Tx) fraction, and the pellet was resuspended in 80 mM Tris-HCl (pH

405   8.0) (PSD fraction).

406

407 **Electron microscopy**

408   Cultured neurons were fixed with 2% glutaraldehyde, 3 mM $CaCl_2$, and 0.1 M cacodylate

409   buffer, pH 7.4, for 1 h. After washes, samples were post-fixed in 2.7% OsO_4 and 167 mM

410   cacodylate, pH 7.4, for 1 h on ice (Kageyama et al., 2014; Wakabayashi et al., 2009). After washes

411   in water, samples were incubated in 2% uranyl acetate for 30 min. After dehydration using 50,

412   70, 90, and 100% ethanol, samples were embedded in EPON resin. Ultrathin sections were

413   obtained using a Reichert-Jung ultracut E, stained with 2% uranyl acetate and 0.3% lead citrate,

414   and viewed using a transmission electron microscope (H-7600; Hitachi) equipped with a dual CCD

415   camera (Advanced Microscopy Techniques).

416   For dynasore treatment, cells were incubated with 80 µM of dynasore (Sigma-Aldrich,

417   D7693) in culture medium for different times, then fixed and further processed for electron

418   microscopy as described above. To stimulate endocytosis through chemical long-term depression

419   (chemical LTD), neurons were incubated with 20 µM of NMDA (Tocris, 0114), 10 µM of glycine

420   (Tocris, 0219), 0.3 mM of $MgCl_2$, 2 mM of $CaCl_2$ and 1 µM of TTX (Tocris, 1078) in Base buffer (10

421   mM HEPES, pH 7.4, 140 mM NaCl, 2.4 mM KCl, 10 mM glucose) for 4 min. As a control, Base

422   buffer containing 2 mM of $MgCl_2$, 2 mM of $CaCl_2$ and 1 µM of TTX was used. To induce chemical

423   LTD in the presence of dynasore, neurons were first incubated for 1 min with 80 µM of dynasore

424   in the culture medium and followed by a 3-min chemical LTD treatment in the presence of

425   dynasore (80 µM). Neurons were then fixed and processed as described above.

426

427   **Analysis of endocytic zone**

428   Hippocampal neurons (DIV22) were transfected with 1 µg of Psd-95.FingR-GFP plasmids

429   (Addgene, 46295) and 250 ng of mCherry-clathrin light chain plasmids (Addgene, 27680) per

430   coverslip in 12-well plates. Two days after transfection, neurons were treated with chemical LTD

431   stimulation, fixed in PBS containing 4% formaldehyde and 4% sucrose for 20 min, washed with

432   PBS and mounted. Neurons were selected based on GFP fluorescence, and mCherry/GFP images

433   were taken. Images were acquired with LSM800 GaAsP laser scanning confocal microscopes and

434   analyzed using ImageJ.

435

Surface biotinylation assay

Cultured neurons were washed once with Base buffer containing 2 mM MgCl$_2$ and 2 mM CaCl$_2$ at room temperature; they were then washed twice with an ice-cold version of the same buffer. Cell-surface proteins were biotinylated with 1 mg/mL sulfo-NHS-SS-biotin (Pierce, 21331) in the same buffer for 20 min on ice. The remaining biotin was quenched by washing the cells two times for 5 min each with ice-cold PBS containing 20 mM glycine, 2 mM MgCl$_2$ and 2 mM CaCl$_2$. Immediately after quenching, the neurons were washed twice with PBS containing 2 mM MgCl$_2$ and 2 mM CaCl$_2$ and then lysed with RIPA buffer that contained cOmplete Mini Protease Inhibitor. The biotinylated cell surface proteins were precipitated using NeutrAvidin agarose (Pierce, 29200). The precipitated proteins and total cell lysates were separated by SDS-PAGE and blotted with antibodies to GluR1, GluR2, GluR3 and GAPDH.

GluR1 internalization assay

Cultured neurons were transfected with 1 μg of Psd-95-mCherry plasmids (Blanpied et al., 2008) and 1 μg of GFP-GluR1 plasmids (Hussain et al., 2014) per coverslip in 12-well plates. Two days after transfection, the neurons were treated with chemical LTD stimulation, fixed in PBS containing 4% formaldehyde and 4% sucrose for 8 min, washed with PBS and blocked in 1% BSA/PBS for 30 min. To label surface GFP-GluR1, the cells were incubated with GFP antibody (Senoo et al., 2019) at 4°C overnight and then treated with Alexa Fluor 647-conjugated secondary antibodies. Images were acquired using LSM800 GaAsP laser scanning confocal microscopes and analyzed using ImageJ. Identical settings were used to acquire each image within an experiment.

458

Transferrin uptake

MEFs were incubated with 5 µg/ml of Alexa-Fluor-647-transferrin (Thermo, T23366) in

the culture medium for 30 min at 4 °C or 37 °C. Cells were washed twice with cold PBS, fixed

using PBS containing 4% paraformaldehyde, washed in PBS and visualized by confocal

microscopy. Mean fluorescent signals in each cell were measured using Image J. Cultured

neurons were incubated with 50 µg/ml of FITC-transferrin (Thermo, T2871) in the culture

medium for 15 min at 4 °C or 37 °C. Cells were washed twice with cold PBS, fixed using PBS

containing 4% paraformaldehyde and 4% sucrose, washed in PBS and then visualized by confocal

microscopy. Mean fluorescent intensity was measured along dendrites (100 µm in length) using

Image J.

***In utero* electroporation**

In utero electroporation that targeted the dorsal hippocampus region was performed

according to our published protocol with some modifications (Saito et al., 2016). Pregnant mice

(C57BL/6J, The Jackson Laboratory, stock no. 000664) were anesthetized at embryonic day 15.5

(E15.5) by intraperitoneal administration of a mixed solution of ketamine HCl (100 mg/kg),

xylazine HCl (7.5 mg/kg), and buprenorphine HCl (0.05 mg/kg). After the uterine horn was

exposed by laparotomy, the CAG promoter-driven eGFP expression plasmid, pCAGGS1-eGFP (1

µg/µl), together with the Drp1$_{ABCD}$ knockdown plasmid, pSUPER-AB (1 µg/µl), was injected (1-2

µl) into the lateral ventricles with a glass micropipette made from a microcapillary tube

(Narishige, Cat #GD-1). Using a ø3mm electrode (Nepagene #CUY650P3), the plasmids were

480   delivered into the dorsal hippocampus by electric pulses (40V; 50 ms), which were charged four

481   times at intervals of 950 ms with an electroporator (Nepagene #CUY21EDIT). After

482   electroporation, the uterine horn was replaced in the abdominal cavity to allow the embryos to

483   continue to develop.

484

485   **Behavioral analysis**

486   All of the behavior tests were performed in mice of 2-5 months of age at the Behavior

487   Core of the Johns Hopkins University School of Medicine. For open field tests, mice were placed

488   in a Photo-beam Activity System Open Field (San Diego Instruments, CA, USA) and their

489   movement was recorded for 30 min (Breu et al., 2016). The open field chamber consisted of a

490   clear Plexiglas box (40 × 40 × 37 cm) with 16 horizontal and 16 vertical photo-beams to assess

491   locomotion and location tendency. Activity parameters were quantified as the number of beam

492   breaks.

493   For PPI tests, mice were put in a clear Plexiglas cylinder (3.8 cm in diameter) within a

494   startle chamber (San Diego Instruments) and tested for their sensorimotor gating function using

495   SR-LAB software (Nasu et al., 2014; Saito et al., 2016) (Startle Response System, San Diego

496   Instruments, CA, USA). A loudspeaker mounted 24 cm above the cylinder provided acoustic

497   stimuli and background noise (70 dB) and controlled the delivery of all stimuli to the animal by

498   SR-LAB software and the interface system. A maximum voltage during the 100-ms period

499   beginning at the stimulus onset was measured as a startle amplitude. To initiate the test, mice

500   were given a 5-min acclimation period with 70 dB background noise; this background noise was

501   present throughout the entire session. After acclimation, mice were exposed to a pulse (a 120

502 dB, 40 ms) 10 times and then the background-only session 10 times at a 20-s inter-stimuli

503 interval (habituation session). In experimental sessions, mice were exposed to the following

504 types of trials: pulse alone trial (a 120-dB, 100-ms broadband burst); the omission of stimuli (no

505 pulse, only background noise); and five prepulse-pulse combination trials. Broadband bursts (20

506 ms) were individually presented as prepulses for 80 ms before the pulse (120-dB, 100-ms

507 broadband pulse). Each session consisted of six presentations of each type of trial presented at a

508 20-s inter-stimulus interval in a pseudorandom order. PPI was defined as a reduced percentage

509 of startle amplitude in prepulse-pulse trials compared to the startle amplitude in startle-alone

510 trials.

511   For the Y-maze test, mice were placed in a Y-shaped maze with three arms (38 × 7.5 × 12

512 cm) at 120-degree angles from each other. After introduction to the center of the maze, mice are

513 allowed to freely explore the three arms and are video-recorded for 10 min. The number of arm

514 entries and the time spent in each arm were scored in order to calculate the percentage of

515 alternation.

516   For rotarod tests, mice were placed on the rod spindle assembly (3.0 cm in diameter) of

517 the Rotamex-5 system (Kageyama et al., 2012) (Columbus Instruments, OH, USA). Mice were first

518 trained at 4.0 rpm for 5 min. After this training session, the rotarod was accelerated with a 1.0

519 rpm increase in rotational speed every 5 s. The time elapsed before falling was recorded for each

520 mouse. Three consecutive trials were performed and the results were averaged in each mouse.

521   For the elevated plus maze test, a mouse was placed on the starting platform in the plus

522 maze (San Diego Instruments Inc., San Diego, CA, USA) and the mouse's behaviors were video-

523   recorded for 5 min. We scored the numbers of entries into the closed and open arms and the

524   time spent in the closed and open arms.

525

526   **MEFs and lentiviruses**

527   Drp1-KO MEFs were cultured in Iscove's modified Dulbecco's medium supplemented with

528   10% fetal bovine serum as described previously (Kageyama et al., 2014). Genotypes of MEFs

529   were confirmed by PCR as described (Kageyama et al., 2014). No contamination of mycoplasma

530   has been confirmed. Lentiviruses were produced as described previously (Itoh et al., 2018).

531

537

540

541   **Figure Legends**

542   **Figure 1. Drp1$_{ABCD}$ is induced during a postnatal period and enriched in postsynaptic terminals.**

543   (A) Domain architecture of Drp1$_{ABCD}$. Alternative exons A and B are present in the 80-loop inside

544   the GTPase domain while alternative exons C and D are located in the variable domain. (B)

545   Different mouse organs were analyzed by Immunoblotting using antibodies to Drp1$_{ABCD}$ (AB),

546   pan-Drp1, the mitochondrial protein PDH, and GAPDH. 60 µg (AB and pan-Drp1) and 12.5 µg

547   (PDH and GAPDH) of proteins were loaded per lane. (C) Whole brains and hippocampi were

548   analyzed at the indicated ages by Immunoblotting with antibodies to Drp1$_{ABCD}$, postsynaptic

549   density protein 95 (Psd-95), pan-Drp1, and actin. (D) Hippocampal neurons were cultured *in vitro*

550   for 1, 2, 3 and 4 weeks and analyzed by immunoblotting. (E) Cultured hippocampal neurons were

551   co-transfected at 3 weeks with plasmids carrying HA-Drp1$_{ABCD}$ or HA-Drp1$_{BCD}$, along with plasmids

552   carrying a cytosolic marker, tdTomato. Three days after transfection, neurons were analyzed by

553   immunofluorescence microscopy with antibodies to RFP (which recognizes tdTomato) and HA.

554   Boxed regions are enlarged. Bar, 20 µm. (F) Intensity of tdTomato (red) and HA (green) signals in

555   dendritic shafts and spines were quantified along the lines shown in Figure 1E. Intensity was

556   normalized to the highest value. (G) Ratios of signal intensity in spines relative to those in

557   dendritic shafts were analyzed for HA-Drp1$_{ABCD}$ and HA-Drp1$_{BCD}$. As a control, the tdTomato signal

558   was used. Bars are mean ± SD (n = 176 spines in 10 neurons expressing HA-Drp1$_{ABCD}$ and 163

559   spines in 10 neurons expressing HA-Drp1$_{BCD}$). (H) Cultured hippocampal neurons were co-

560   transfected at 3 weeks with plasmids carrying tdTomato and HA-Drp1$_{ABCD}$ or HA-Drp1$_{BCD}$ and

561   subjected to immunofluorescence microscopy with antibodies to HA and vesicular glutamate

562   transporter 1 (VGLUT1). Boxed regions are enlarged. Bar, 5 µm. (I) Postsynaptic density fractions

563   were isolated from the whole brains of wild-type mice and analyzed by Immunoblotting. Brain,

564   whole brain; P2, membrane fraction; S2, cytosolic fraction; Syn, total synaptosomal fraction;

565   Syn/Tx, Triton-soluble synaptosomal fraction; PSD, postsynaptic density fraction. (J) Band

566   intensity of total Drp1 (pan-Drp1) and Drp1$_{ABCD}$ (AB) in the postsynaptic density fraction was

567   quantified relative to the whole brain. Bars are mean ± SD (n = 3). Statistical analysis was

568   performed using Mann–Whitney U test (G) and Student's t-test (J). n.s., not significant.

569   The following source data is available for figure 1:

570   **Source data 1.** Drp1$_{ABCD}$ is enriched in postsynaptic terminals.

571

572   **Figure 2. The loss of Drp1$_{ABCD}$ blocks postsynaptic endocytosis.** (A) Two guide RNAs were used to

573   cut the genome at two positions (red arrowheads) to remove the majority of exon A and part of

574   the following intron using CRISPR/Cas9. This deletion introduced a stop codon 20 residues

575   downstream from the deletion site (STOP). (B) The indicated tissues were harvested from control

576   and Drp1$_{exonA}$-KO mice and analyzed by immunoblotting using antibodies to Drp1$_{ABCD}$ (AB), pan-

577   Drp1, the mitochondrial protein PDH, and GAPDH. (C and D) Weights of the whole body (C) and

578   brain (D) were measured. Bars are mean ± SD (n = 4 in C and 5 in D). (E) Images of the whole

579   brain. Bar, 1 cm. (F) H&E staining of cerebella of control and Drp1$_{exonA}$-KO mice. Sagittal sections

580   were cut in the midline. Bar, 1 mm. (G) Frozen sections of the hippocampus in control and

581   Drp1$_{exonA}$-KO mice were stained with DAPI. Bar, 0.5 mm. The thickness of the CA1 layer was

582   measured. Bars are mean ± SD (n = 3). (H) Control and Drp1$_{exonA}$-KO hippocampal neurons were

583   cultured for 3 weeks and subjected to transmission electron microscopy. An arrowhead indicates

584   a clathrin-coated pit (CCP) at a postsynaptic terminal. Bar, 100 nm. (I and J) Quantification of the

585   number of CCPs at postsynaptic and presynaptic terminals. Bars are mean ± SD (n = 4

586   experiments, in which 167, 196, 172, 191 control and 158, 161, 169, 221 Drp1$_{exonA}$-KO synapses

587   were analyzed). (K and L) The numbers of CCPs with three different morphologies (shallow, U-

588   shaped, and Omega-shaped) were measured. Bar, 100 nm. (M-P) Control and Drp1$_{exonA}$-KO

589   hippocampal neurons were treated with 80 µM of dynasore for 30 min and analyzed by electron

590   microscopy (M and O). Bar, 500 nm. The number of CCPs (N) and the size of mitochondria (P)

591   were determined. Bars are mean ± SD (n = 159, 182, 172 -/control, 152, 163, 143 +/control, 176,

592   163, 129 -/KO, and 162, 146, 145 +/KO synapses) (N) and (n = 30-32 mitochondria analyzed in

593   each group) (P). (Q and R) Chemical long-term depression (NMDA/Gly) was induced by NMDA for

594   3 min in the presence or absence dynasore (80 µM). Neurons were then fixed, and CCPs at

595   postsynaptic and presynaptic terminals were analyzed by electron microscopy. Bars are mean ±

596   SD (n = 3-4 experiments. In each experiment, more than 100 synapses were analyzed). Statistical

597   analysis was performed using Student's *t*-test (C, D, G, I, J, L and N) and One-way ANOVA with

598   post-hoc Tukey (P, Q and R). (S) Summary of the data.

599   The following source data and figure supplements are available for figure 2:

600   **Source data 1.** The loss of Drp1$_{ABCD}$ blocks postsynaptic endocytosis.

601   **Figure supplement 1.** Dynasore does not affect mitochondrial morphology in cells.

602

603   **Figure 3. The endocytic zone is mislocalized in Drp1$_{exonA}$-KO neurons.** (A and B) Hippocampal

604   neurons were cultured and transfected with plasmids expressing Psd-95.FingR-GFP and mCherry-

605   CLC. Two days after transfection, neurons were subjected to chemical LTD stimulation

606   (NMDA/Gly), fixed and analyzed by laser scanning confocal microscopy. Bar, 5 µm. The number

607   of Psd-95.FingR-GFP signals that are not associated with mCherry-CLC was scored. Bars are mean

608   ± SD (n = 14-15 neurons were analyzed in each group). (C) Cell surface proteins were biotinylated

609   with sulfo-NHS-SS-biotin in cultured control and Drp1$_{exonA}$-KO hippocampal neurons. The neurons

610   were lysed and incubated with NeutrAvidin agarose. Total cell lysates and precipitated proteins

611   (Surface) were separated by immunoblotting to antibodies to GluR1, GluR2, GluR3 and GAPDH.

612   (D) Band intensity was determined. Bars are mean ± SD (n = 5). (E) Cultured neurons were co-

613   transfected with plasmids carrying Psd-95-mCherry and GFP-GluR1. Two days after transfection,

614   the neurons were treated with chemical LTD (NMDA/Gly) and subjected to immunofluorescence

615   microscopy with anti-GFP antibodies without permeabilization of the plasma membrane. Images

616   were acquired using identical settings. (F) The relative intensity of the signal from the anti-GFP

617   antibodies (surface GFP-GluR1) compared with the GFP signal (total GFP-GluR1) was determined.

618   Bars are mean ± SD (n = 50). (G) Model for the function of Drp1$_{ABCD}$ in the postsynaptic terminal.

619   (H-J) Control and Drp1$_{exonA}$-KO hippocampal neurons were subjected to immunofluorescence

620   microscopy with antibodies against the mitochondrial protein PDH. Boxed regions are enlarged:

621   a, proximal dendritic regions and b, distal dendritic regions. Bar, 20 μm. The length of

622   mitochondria was determined in proximal (I) and distal dendritic regions (J). Bars are mean ± SD

623   (n = 10 neurons analyzed in each group. 70-120 mitochondria measured in each neuron).

624   Statistical analysis was performed using Kruskal-Wallis test with Dunn's multiple comparisons

625   test (B), Mann–Whitney *U* test (I) and Student's *t*-test (D, F and J).

626   The following source data and figure supplements are available for figure 3:

627   **Source data 1.** The endocytic zone is mislocalized in Drp1$_{exonA}$-KO neurons.

628   **Figure supplement 1**. Analysis of transferrin uptake.

629

630   **Figure 4. The loss of Drp1$_{ABCD}$ increases dendrite growth and sensorimotor gating.** (A) Control

631   and Drp1$_{exonA}$-KO hippocampal neurons were cultured and transfected with plasmids expressing

632   GFP at 3 weeks. Boxed regions are enlarged. Arrowheads indicate axons that lack dendritic

633   spines. Bar, 20 μm. (B and C) The numbers of primary dendrites (B) and dendritic branches (C)

634   were quantified. Bars are mean ± SD (n = 60 control and 59 KO neurons). (D) The number of

635   spines was quantified (n = 10 control and 10 KO neurons). (E) The DNA sequence that is targeted

636   to knock down Drp1$_{ABCD}$ is shown. (F) HEK293 cells were co-transfected with plasmids carrying

637   the indicated GFP-Drp1 and shRNAs. Whole-cell extracts were analyzed by Immunoblotting using

638   the indicated antibodies. (G) Mouse hippocampal neurons were cultured for 2 or 3 weeks and

639   transfected with plasmids expressing the indicated shRNAs and GFP as a cytosolic marker. Images

640   of 3-week cultured neurons are presented. Boxed regions are enlarged. Arrowheads indicate

641   axons that lack dendritic spines. Bar, 20 μm. (H) The number of primary dendrites were

642   quantified. Bars are mean ± SD (n = 29-30 neurons at 2 weeks and 50 neurons at 3 weeks). (I)

643   Cultured neurons were transfected at 3 weeks with the plasmid expressing AB-targeted shRNA

644   and GFP along with another plasmid carrying shRNA-resistant Drp1$_{ABCD}$. The number of primary

645   dendrites was quantified. Bars are mean ± SD (n = 60 neurons for empty plasmid and 52 for

646   Drp1$_{ABCD}$). (J) Cultured hippocampal neurons were transfected with the indicated shRNA plasmids

647   that co-express GFP in the presence or absence of 2 μM tetrodotoxin (TTX). The number of

648   primary dendrites was quantified (n = 60 for -TTX/scramble, 75 for +TTX/scramble, 79 for -

649   TTX/AB and 57 for +TTX/AB). (K and L) Control and Drp1$_{exonA}$-KO mice were crossed with a mouse

650   line expressing cytosolic GFP from the neuron-specific Thy1 promoter. We analyzed the number

651   of neurites in the hippocampus (K) and cortex (L) at the age of 3-4 months. Bars are mean ± SD (n

652   = 90 neurons in 3 mice for each genotype). Bar, 10 μm. (M) Plasmids carrying the indicated

653   shRNAs were introduced into the hippocampi of E15.5 mouse embryos, along with plasmids

654   carrying GFP, by electroporation *in utero*. (N) Hippocampi were analyzed at an age of 7 weeks

655 using laser confocal microscopy of frozen brain sections. Bar, 20 μm. The number of neurites that

656 directly emerge from the soma was quantified. Bars are mean ± SD (n = 51 neurons for scramble

657 and 56 for AB-targeted). (O and P) Startle response (O) and PPI tests (P). Bars are mean ± SD (n =

658 12 control and 14 KO mice). Statistical analysis was performed using Student's t-test (B, C, D. H-3

659 weeks, I, K, N and P), Mann–Whitney U test (H-2 weeks, L and O) and One-way ANOVA with post-

660 hoc Tukey (J).

661 The following source data and figure supplements are available for figure 4:

662 **Source data 1.** The loss of Drp1$_{ABCD}$ increases dendrite growth and sensorimotor gating.

663 **Figure supplement 1.** The number of axons is not affected by Drp1$_{ABCD}$ knockdown.

664 **Figure supplement 2.** The expression of GFP from the Thy1 promoter.

665 **Figure supplement 3.** Behavior analysis of Drp1$_{exonA}$-KO mice.

666 **Figure supplement 4.** The localization of Drp1$_{ABCD}$ at the plasma membrane is insensitive to

667 dynasore treatment.

668

669 **Supplementary Figure Legends**

670 **Figure 2—figure supplement 1. Dynasore does not affect mitochondrial morphology in cells.**

671 (A-C) Cultured control and Drp1$_{exonA}$-KO neurons were incubated with 80 μM of dynasore for 30

672 min and analyzed using immunofluorescence microscopy with anti-PDH antibodies. Boxed

673 regions are enlarged: a, proximal dendritic regions and b, distal dendritic regions. Bar, 20 μm.

674 Mitochondrial length was determined in the proximal (B) and distal dendritic regions (C). Bars are

675 mean ± SD (n = 10 neurons analyzed in each group; 99–121 mitochondria were measured in each

676 neuron). The statistical analysis was performed using the Student's t-test. (D) WT MEFs were

677   treated with 80 µM of dynasore for 1 hour and analyzed by immunofluorescence microscopy

678   with anti-Tom20 antibodies (BD Biosciences, 61278). As a control for the loss of Drp1 function,

679   Drp1-KO MEFs were also examined. Bar, 20 µm. (E) Mitochondrial shape is quantified (n = 30

680   cells).

681

682   **Figure 3—figure supplement 1. Analysis of transferrin uptake.** (A) Cultured control and

683   Drp1$_{exonA}$-KO neurons were incubated with 50 µg/ml FITC-transferrin for 15 min at 4 °C or 37 °C.

684   Cells were washed with cold PBS, fixed with paraformaldehyde and viewed by confocal

685   microscopy. Intensity of FITC signals was quantified (n = 10 control neurons and 6 KO neurons).

686   Statistical analysis was performed using Student's *t*-test. (B) Drp1-KO MEFs expressing no Drp1,

687   Drp1$_{ABCD}$ or Drp1$_{BCD}$ were incubated with 5 µg/ml of Alexa-Fluor-647-transferrin for 30 min at 4

688   °C or 37 °C. After fixation, cells were visualized by confocal microscopy. Intensity of Alexa-Fluor-

689   647 signals was quantified. Bars are mean ± SD (n = 15-25 cells analyzed in each group).

690   Statistical analysis was performed using one-way ANOVA with post-hoc Tukey. (F) The

691   localization of Drp1$_{ABCD}$ at the plasma membrane is insensitive to dynasore treatment. Drp1-KO

692   MEFs were transduced with lentiviruses expressing Drp1$_{ABCD}$, treated with 80 µM dynasore for 1

693   hour and analyzed by immunofluorescence microscopy with antibodies to Drp1 and Tom20. Bar,

694   20 µm. The number of cells that show the localization of Drp1$_{ABCD}$ at the plasma membrane was

695   quantified (n = 3 experiments. 30-60 cells were analyzed in each experiment). Statistical analysis

696   was performed using Student's *t*-test.

697

698   **Figure 4—figure supplement 1. The number of axons is not affected by Drp1$_{ABCD}$ knockdown.**

699　Cultured hippocampal neurons were transfected at 3 weeks with the indicated shRNA plasmids

700　carrying GFP as a cytosolic marker. Cells were subjected to immunofluorescence microscopy with

701　anti-MAP2 antibodies. Arrowheads indicate axons, and arrows indicate dendrites. Bar, 20 μm.

702

703　**Figure 4—figure supplement 2. The expression of GFP from the Thy1 promoter.** Frozen section

704　of the hippocampus (A) and cortex (B) in control and Drp1$_{exonA}$-KO mice expressing cytosolic GFP

705　from the neuron-specific Thy1 promoter are shown. Bar, 100 μm.

706

707　**Figure 4—figure supplement 3. Behavior analysis of Drp1$_{exonA}$-KO mice.** (A) Open field test. Total

708　activity (Locomotor activity) and percentage time spent in the central and peripheral regions

709　(Anxiety). (B) Y-maze tests. Number of arm entries (Locomotor activity), spontaneous alternation

710　(Working memory), and time in novel arm (Spatial recognition memory) were determined. (C)

711　Rotarod test. (D) Elevated plus maze tests. Bars are mean ± SD (n = 26 control and 26 Drp1$_{exonA}$-

712　KO mice). Statistical analysis was performed using Student's *t*-test.

713

714　**Source Data File List for Figures (file name)**

715　Figure 1–Source Data 1 (Itoh et al_Fig1-data1.xlsx)

716　Figure 2–Source Data 1 (Itoh et al_Fig2-data1.xlsx)

717　Figure 2–figure supplement 1–Source Data 1 (Itoh et al_Fig2-S1-data1.xlsx)

718　Figure 3–Source Data 1 (Itoh et al_Fig3-data1.xlsx)

719　Figure 3–figure supplement 1–Source Data 1 (Itoh et al_Fig3-S1-data1.xlsx)

720　Figure 4–Source Data 1 (Itoh et al_Fig4-data1.xlsx)

721   Figure 4–figure supplement 3–Source Data 1 (Itoh et al_Fig4-S3-data1.xlsx)

722

723   **References**

724   Adachi, Y., Itoh, K., Yamada, T., Cerveny, K.L., Suzuki, T.L., Macdonald, P., Frohman, M.A.,
725   Ramachandran, R., Iijima, M., and Sesaki, H. (2016). Coincident Phosphatidic Acid Interaction
726   Restrains Drp1 in Mitochondrial Division. Mol Cell *63*, 1034-1043.
727   Araki, Y., Lin, D.T., and Huganir, R.L. (2010). Plasma membrane insertion of the AMPA receptor
728   GluA2 subunit is regulated by NSF binding and Q/R editing of the ion pore. Proc Natl Acad Sci U S
729   A *107*, 11080-11085.
730   Araki, Y., Zeng, M., Zhang, M., and Huganir, R.L. (2015). Rapid dispersion of SynGAP from synaptic
731   spines triggers AMPA receptor insertion and spine enlargement during LTP. Neuron *85*, 173-189.
732   Berthet, A., Margolis, E.B., Zhang, J., Hsieh, I., Hnasko, T.S., Ahmad, J., Edwards, R.H., Sesaki, H.,
733   Huang, E.J., and Nakamura, K. (2014). Loss of mitochondrial fission depletes axonal mitochondria
734   in midbrain dopamine neurons. The Journal of neuroscience : the official journal of the Society
735   for Neuroscience *34*, 14304-14317.
736   Blanpied, T.A., Kerr, J.M., and Ehlers, M.D. (2008). Structural plasticity with preserved topology in
737   the postsynaptic protein network. Proc Natl Acad Sci U S A *105*, 12587-12592.
738   Breu, M., Zhang, J., Porambo, M., Pletnikov, M.V., Goeral, K., Kakara, M., Johnston, M.V., and
739   Fatemi, A. (2016). Diffusion Tensor Imaging Abnormalities in the Cerebral White Matter Correlate
740   with Sex-Dependent Neurobehavioral Deficits in Adult Mice with Neonatal Ischemia. Dev
741   Neurosci *38*, 83-95.
742   Cho, D.H., Nakamura, T., and Lipton, S.A. (2010). Mitochondrial dynamics in cell death and
743   neurodegeneration. Cell Mol Life Sci *67*, 3435-3447.
744   Divakaruni, S.S., Van Dyke, A.M., Chandra, R., LeGates, T.A., Contreras, M., Dharmasri, P.A.,
745   Higgs, H.N., Lobo, M.K., Thompson, S.M., and Blanpied, T.A. (2018). Long-Term Potentiation
746   Requires a Rapid Burst of Dendritic Mitochondrial Fission during Induction. Neuron *100*, 860-875
747   e867.
748   Fahrner, J.A., Liu, R., Perry, M.S., Klein, J., and Chan, D.C. (2016). A novel de novo dominant
749   negative mutation in DNM1L impairs mitochondrial fission and presents as childhood epileptic
750   encephalopathy. Am J Med Genet A *170*, 2002-2011.
751   Feng, G., Mellor, R.H., Bernstein, M., Keller-Peck, C., Nguyen, Q.T., Wallace, M., Nerbonne, J.M.,
752   Lichtman, J.W., and Sanes, J.R. (2000). Imaging neuronal subsets in transgenic mice expressing
753   multiple spectral variants of GFP. Neuron *28*, 41-51.
754   Friedman, J.R., and Nunnari, J. (2014). Mitochondrial form and function. Nature *505*, 335-343.
755   Gerber, S., Charif, M., Chevrollier, A., Chaumette, T., Angebault, C., Kane, M.S., Paris, A., Alban, J.,
756   Quiles, M., Delettre, C.*, et al.* (2017). Mutations in DNM1L, as in OPA1, result indominant optic
757   atrophy despite opposite effectson mitochondrial fusion and fission. Brain *140*, 2586-2596.
758   Gross, G.G., Junge, J.A., Mora, R.J., Kwon, H.B., Olson, C.A., Takahashi, T.T., Liman, E.R., Ellis-
759   Davies, G.C., McGee, A.W., Sabatini, B.L.*, et al.* (2013). Recombinant probes for visualizing
760   endogenous synaptic proteins in living neurons. Neuron *78*, 971-985.

761 Hussain, N.K., Diering, G.H., Sole, J., Anggono, V., and Huganir, R.L. (2014). Sorting Nexin 27
762 regulates basal and activity-dependent trafficking of AMPARs. Proc Natl Acad Sci U S A *111*,
763 11840-11845.
764 Igarashi, A., Itoh, K., Yamada, T., Adachi, Y., Kato, T., Murata, D., Sesaki, H., and Iijima, M. (2018).
765 Nuclear PTEN deficiency causes microcephaly with decreased neuronal soma size and increased
766 seizure susceptibility. J Biol Chem *293*, 9292-9300.
767 Ishihara, N., Nomura, M., Jofuku, A., Kato, H., Suzuki, S.O., Masuda, K., Otera, H., Nakanishi, Y.,
768 Nonaka, I., Goto, Y.*, et al.* (2009). Mitochondrial fission factor Drp1 is essential for embryonic
769 development and synapse formation in mice. Nature cell biology *11*, 958-966.
770 Itoh, K., Adachi, Y., Yamada, T., Suzuki, T.L., Otomo, T., McBride, H.M., Yoshimori, T., Iijima, M.,
771 and Sesaki, H. (2018). A brain-enriched Drp1 isoform associates with lysosomes, late endosomes,
772 and the plasma membrane. J Biol Chem *293*, 11809-11822.
773 Itoh, K., Nakamura, K., Iijima, M., and Sesaki, H. (2013). Mitochondrial dynamics in
774 neurodegeneration. Trends in Cell Biology *23*, 64-71.
775 Kageyama, Y., Hoshijima, M., Seo, K., Bedja, D., Sysa-Shah, P., Andrabi, S.A., Chen, W., Hoke, A.,
776 Dawson, V.L., Dawson, T.M.*, et al.* (2014). Parkin-independent mitophagy requires Drp1 and
777 maintains the integrity of mammalian heart and brain. The EMBO journal *33*, 2798-2813.
778 Kageyama, Y., Zhang, Z., Roda, R., Fukaya, M., Wakabayashi, J., Wakabayashi, N., Kensler, T.W.,
779 Reddy, P.H., Iijima, M., and Sesaki, H. (2012). Mitochondrial division ensures the survival of
780 postmitotic neurons by suppressing oxidative damage. The Journal of cell biology *197*, 535-551.
781 Kameoka, S., Adachi, Y., Okamoto, K., Iijima, M., and Sesaki, H. (2018). Phosphatidic Acid and
782 Cardiolipin Coordinate Mitochondrial Dynamics. Trends Cell Biol *28*, 67-76.
783 Kandimalla, R., and Reddy, P.H. (2016). Multiple faces of dynamin-related protein 1 and its role in
784 Alzheimer's disease pathogenesis. Biochimica et biophysica acta *1862*, 814-828.
785 Kashatus, D.F. (2018). The regulation of tumor cell physiology by mitochondrial dynamics.
786 Biochem Biophys Res Commun *500*, 9-16.
787 Kraus, F., and Ryan, M.T. (2017). The constriction and scission machineries involved in
788 mitochondrial fission. J Cell Sci *130*, 2953-2960.
789 Lee, Y., and Davis, M. (1997). Role of the hippocampus, the bed nucleus of the stria terminalis,
790 and the amygdala in the excitatory effect of corticotropin-releasing hormone on the acoustic
791 startle reflex. J Neurosci *17*, 6434-6446.
792 Li, H., Alavian, K.N., Lazrove, E., Mehta, N., Jones, A., Zhang, P., Licznerski, P., Graham, M., Uo, T.,
793 Guo, J.*, et al.* (2013). A Bcl-xL-Drp1 complex regulates synaptic vesicle membrane dynamics
794 during endocytosis. Nature cell biology *15*, 773-785.
795 Lu, J., Helton, T.D., Blanpied, T.A., Racz, B., Newpher, T.M., Weinberg, R.J., and Ehlers, M.D.
796 (2007). Postsynaptic positioning of endocytic zones and AMPA receptor cycling by physical
797 coupling of dynamin-3 to Homer. Neuron *55*, 874-889.
798 Macia, E., Ehrlich, M., Massol, R., Boucrot, E., Brunner, C., and Kirchhausen, T. (2006). Dynasore,
799 a cell-permeable inhibitor of dynamin. Dev Cell *10*, 839-850.
800 Nasu, M., Yada, S., Igarashi, A., Sutoo, D., Akiyama, K., Ito, M., Yoshida, N., and Ueda, S. (2014).
801 Mammalian-specific sequences in pou3f2 contribute to maternal behavior. Genome Biol Evol *6*,
802 1145-1156.
803 Pernas, L., and Scorrano, L. (2016). Mito-Morphosis: Mitochondrial Fusion, Fission, and Cristae
804 Remodeling as Key Mediators of Cellular Function. Annual review of physiology *78*, 505-531.

805 Prudent, J., and McBride, H.M. (2017). The mitochondria-endoplasmic reticulum contact sites: a
806 signalling platform for cell death. Curr Opin Cell Biol *47*, 52-63.
807 Ramachandran, R. (2018). Mitochondrial dynamics: The dynamin superfamily and execution by
808 collusion. Semin Cell Dev Biol *76*, 201-212.
809 Roy, M., Reddy, P.H., Iijima, M., and Sesaki, H. (2015). Mitochondrial division and fusion in
810 metabolism. Current opinion in cell biology *33C*, 111-118.
811 Saito, A., Taniguchi, Y., Rannals, M.D., Merfeld, E.B., Ballinger, M.D., Koga, M., Ohtani, Y., Gurley,
812 D.A., Sedlak, T.W., Cross, A.*, et al.* (2016). Early postnatal GABAA receptor modulation reverses
813 deficits in neuronal maturation in a conditional neurodevelopmental mouse model of DISC1. Mol
814 Psychiatry *21*, 1449-1459.
815 Santoro, A., Campolo, M., Liu, C., Sesaki, H., Meli, R., Liu, Z.W., Kim, J.D., and Diano, S. (2017).
816 DRP1 Suppresses Leptin and Glucose Sensing of POMC Neurons. Cell Metab *25*, 647-660.
817 Senoo, H., Kamimura, Y., Kimura, R., Nakajima, A., Sawai, S., Sesaki, H., and Iijima, M. (2019).
818 Phosphorylated Rho-GDP directly activates mTORC2 kinase towards AKT through dimerization
819 with Ras-GTP to regulate cell migration. Nat Cell Biol *21*, 867-878.
820 Serasinghe, M.N., and Chipuk, J.E. (2017). Mitochondrial Fission in Human Diseases. Handb Exp
821 Pharmacol.
822 Shields, L.Y., Kim, H., Zhu, L., Haddad, D., Berthet, A., Pathak, D., Lam, M., Ponnusamy, R., Diaz-
823 Ramirez, L.G., Gill, T.M.*, et al.* (2015). Dynamin-related protein 1 is required for normal
824 mitochondrial bioenergetic and synaptic function in CA1 hippocampal neurons. Cell death &
825 disease *6*, e1725.
826 Strack, S., Wilson, T.J., and Cribbs, J.T. (2013). Cyclin-dependent kinases regulate splice-specific
827 targeting of dynamin-related protein 1 to microtubules. The Journal of cell biology *201*, 1037-
828 1051.
829 Swerdlow, N.R., Geyer, M.A., and Braff, D.L. (2001). Neural circuit regulation of prepulse
830 inhibition of startle in the rat: current knowledge and future challenges. Psychopharmacology
831 (Berl) *156*, 194-215.
832 Tamura, Y., Itoh, K., and Sesaki, H. (2011). SnapShot: Mitochondrial dynamics. Cell *145*, 1158.
833 van der Bliek, A.M., Shen, Q., and Kawajiri, S. (2013). Mechanisms of mitochondrial fission and
834 fusion. Cold Spring Harb Perspect Biol *5*.
835 Vanstone, J.R., Smith, A.M., McBride, S., Naas, T., Holcik, M., Antoun, G., Harper, M.E., Michaud,
836 J., Sell, E., Chakraborty, P.*, et al.* (2015). DNM1L-related mitochondrial fission defect presenting
837 as refractory epilepsy. European journal of human genetics : EJHG.
838 Wakabayashi, J., Zhang, Z., Wakabayashi, N., Tamura, Y., Fukaya, M., Kensler, T.W., Iijima, M.,
839 and Sesaki, H. (2009). The dynamin-related GTPase Drp1 is required for embryonic and brain
840 development in mice. J Cell Biol *186*, 805-816.
841 Waterham, H.R., Koster, J., van Roermund, C.W., Mooyer, P.A., Wanders, R.J., and Leonard, J.V.
842 (2007). A lethal defect of mitochondrial and peroxisomal fission. N Engl J Med *356*, 1736-1741.
843 Widlansky, M.E., and Hill, R.B. (2018). Mitochondrial regulation of diabetic vascular disease: an
844 emerging opportunity. Transl Res *202*, 83-98.
845 Wong, R.O., and Ghosh, A. (2002). Activity-dependent regulation of dendritic growth and
846 patterning. Nat Rev Neurosci *3*, 803-812.
847 Yamada, T., Murata, D., Adachi, Y., Itoh, K., Kameoka, S., Igarashi, A., Kato, T., Araki, Y., Huganir,
848 R.L., Dawson, T.M.*, et al.* (2018). Mitochondrial Stasis Reveals p62-Mediated Ubiquitination in

849   Parkin-Independent Mitophagy and Mitigates Nonalcoholic Fatty Liver Disease. Cell Metab *28*,
850   588-604.
851   Youle, R.J., and van der Bliek, A.M. (2012). Mitochondrial fission, fusion, and stress. Science *337*,
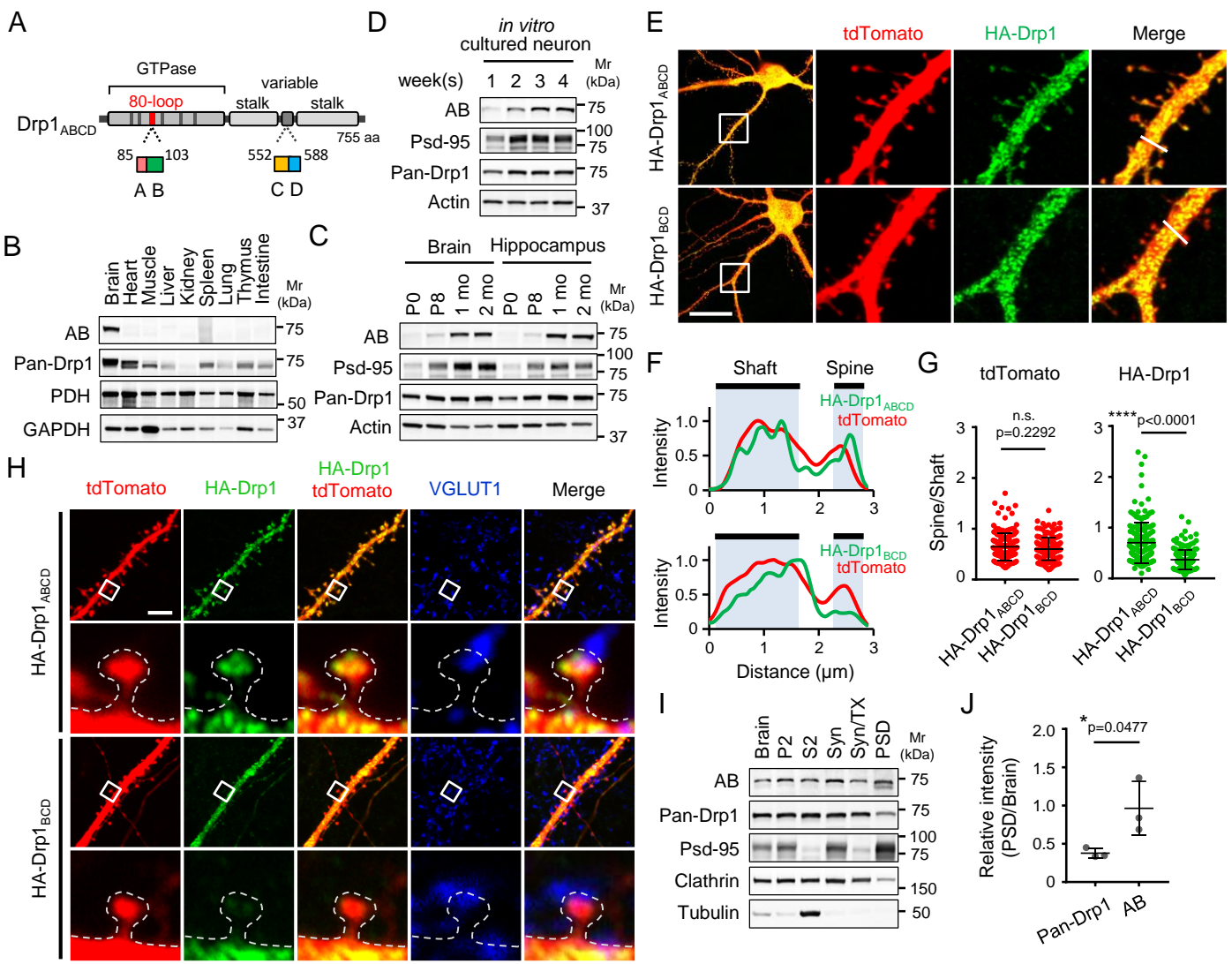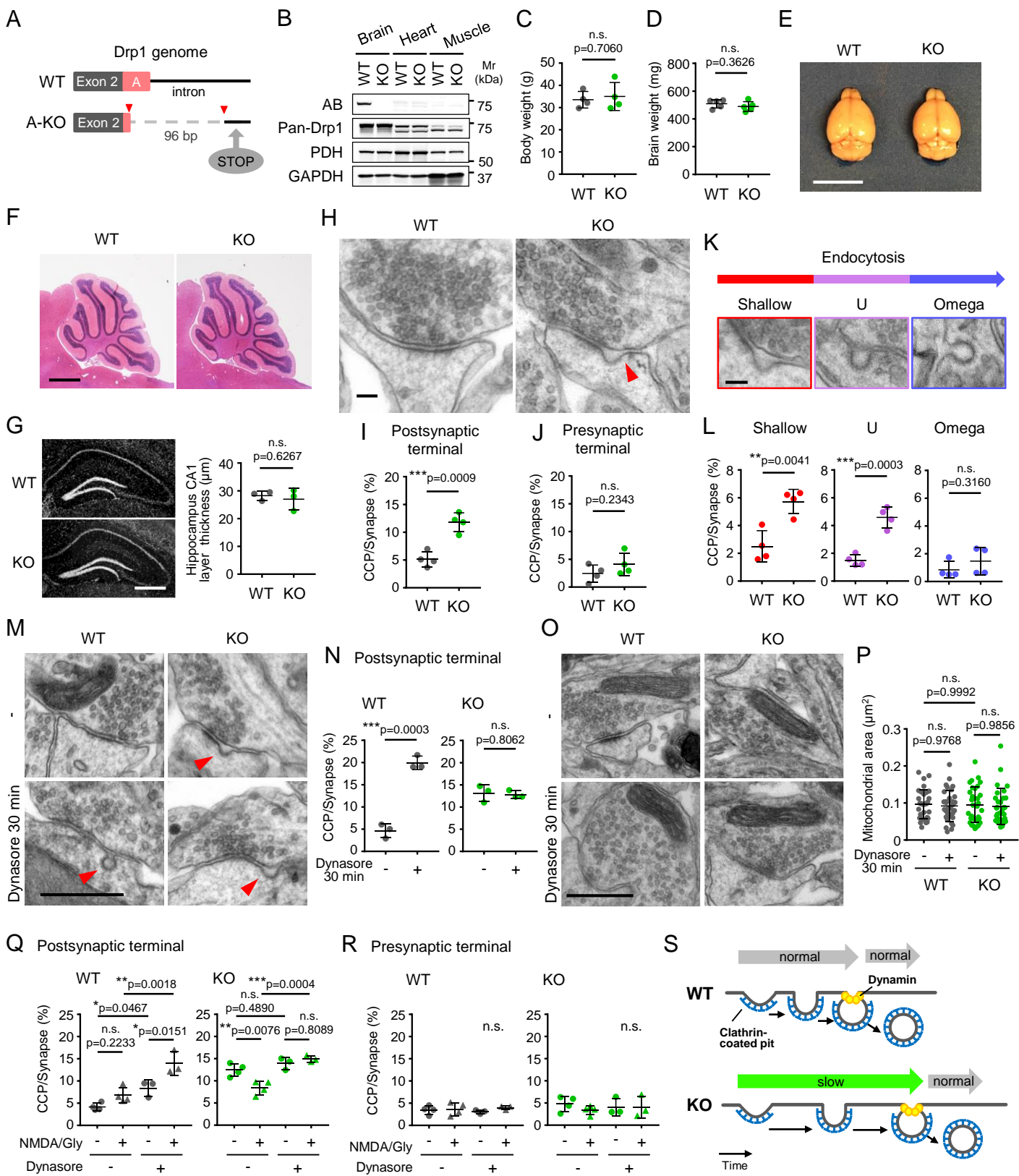852   1062-1065.
853

Figure 1. Itoh *et al.*
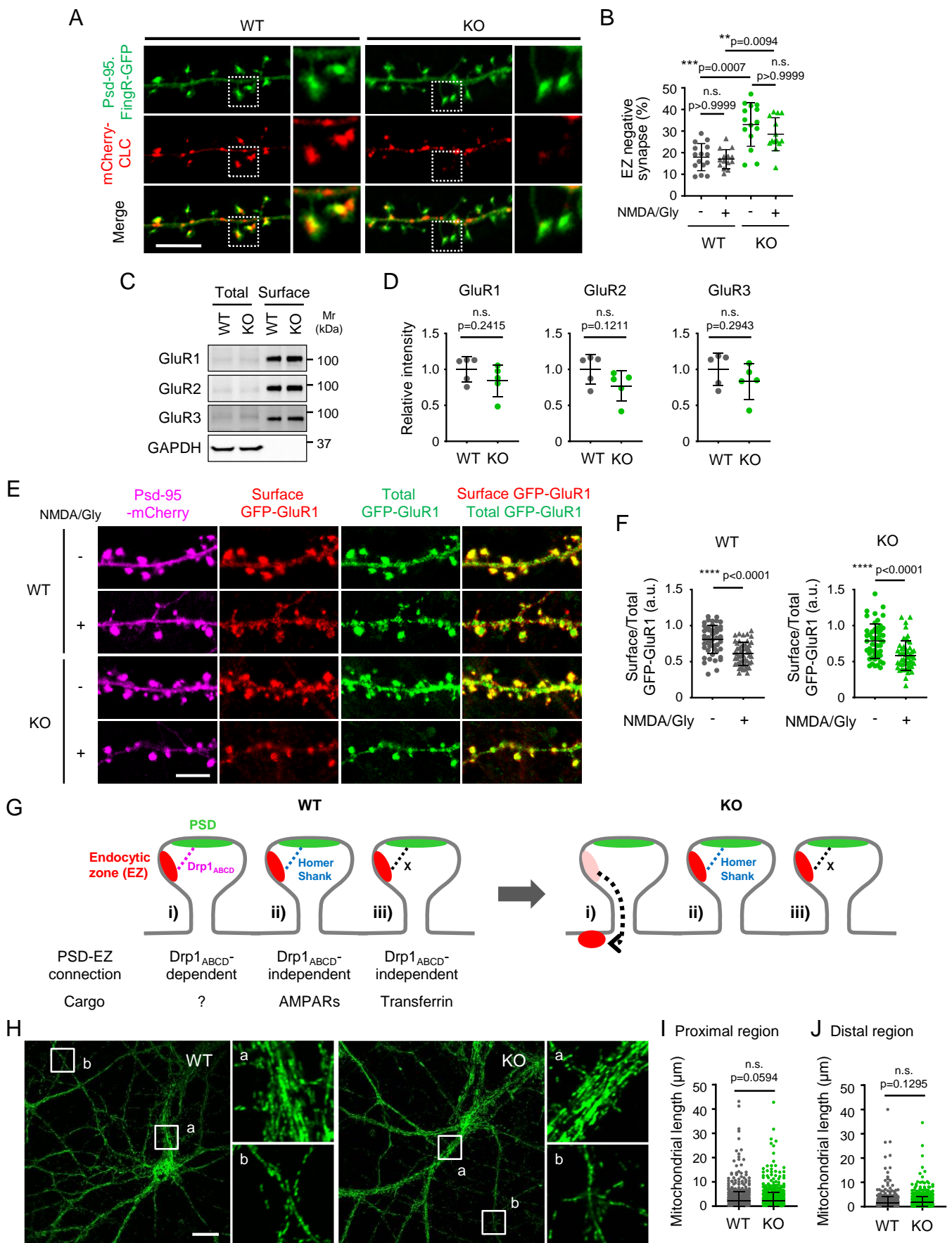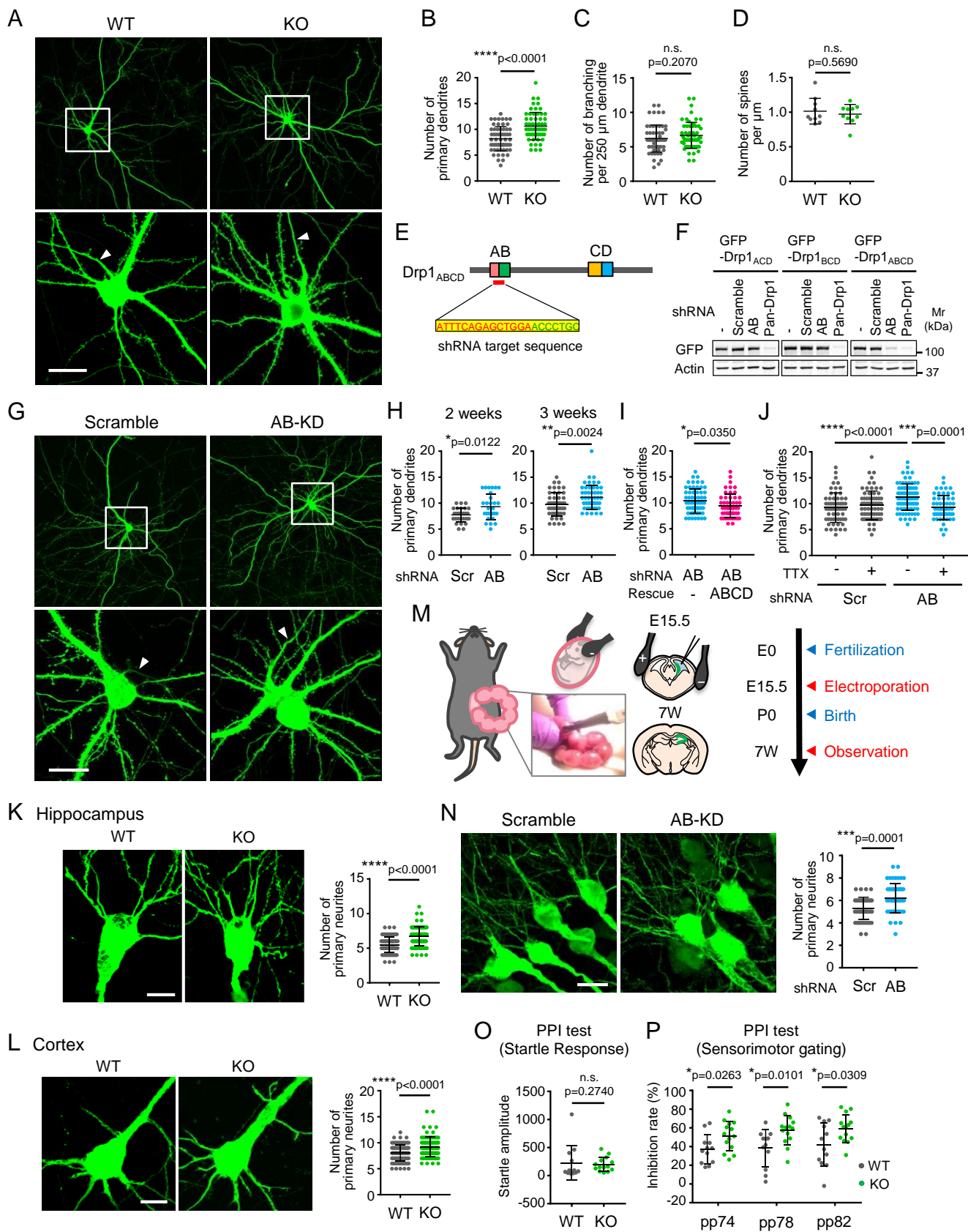
Figure 2. Itoh *et al.*

Figure 3. Itoh *et al.*

Figure 4. Itoh *et al.*

A

- / Dynasore 30 min

B Proximal region

C Distal region

a / b

D

WT MEF / Drp1-KO MEF

Dynasore 1 h: - / + / -

Tom20

E

Mitochondrial shape

Dynasore 1 h: - / + / -

WT / Drp1-KO

elongated / intermediate

F

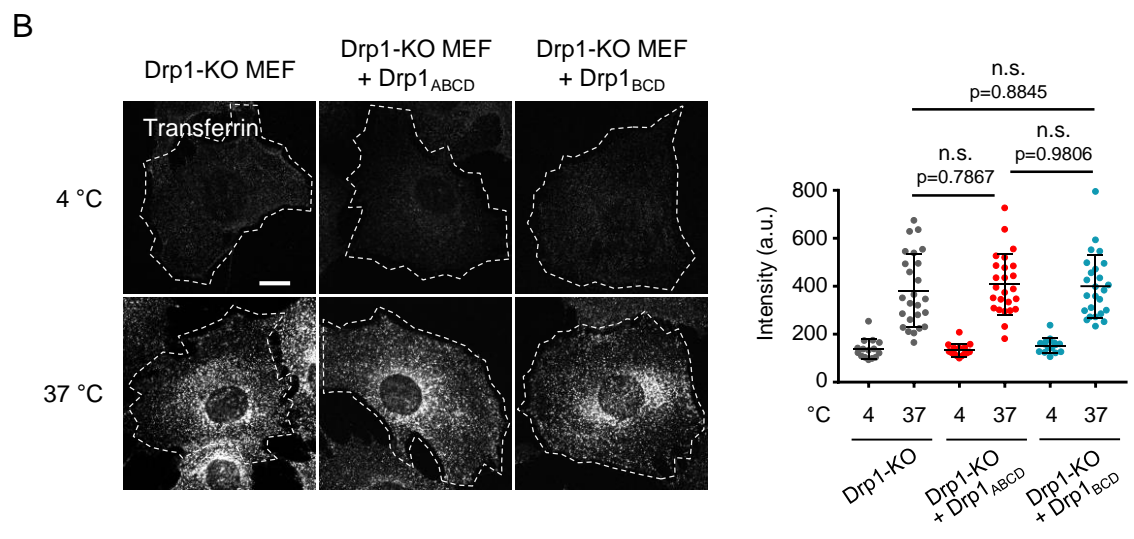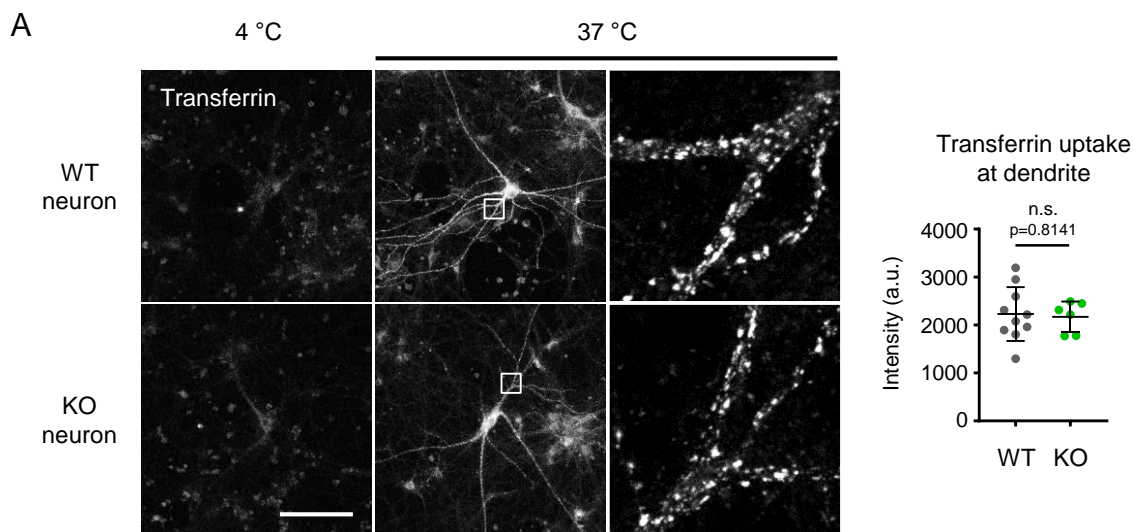Drp1-KO MEF + Drp1$_{ABCD}$

Dynasore 1 h: - / +

Tom20 Drp1$_{ABCD}$

PM localization

n.s. p=0.5701

Figure 2 — figure supplement 1. Itoh *et al.*

A

Figure 3 — figure supplement 1. Itoh *et al.*

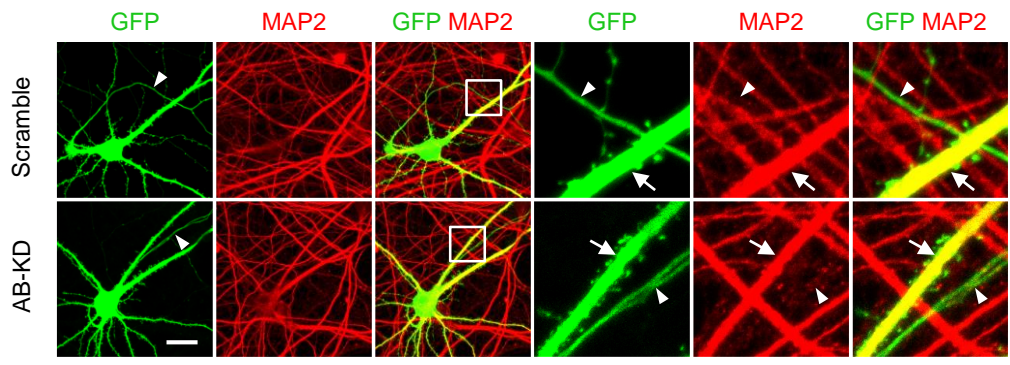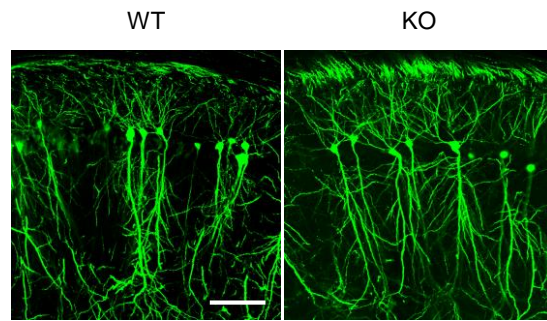Figure 4 — figure supplement 1. Itoh *et al.*

A Hippocampus

WT   KO

B Cortex

WT   KO

Figure 4 — figure supplement 2. Itoh *et al.*

A

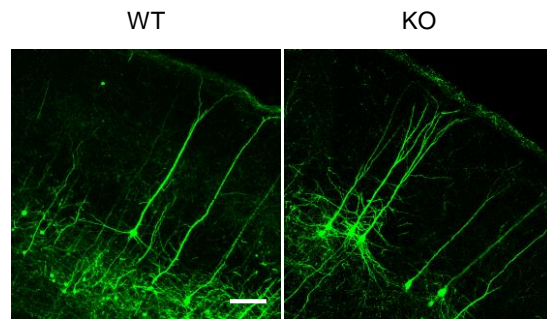**Open filed test (Locomotor activity)**

Open field test (Anxiety)

B

Y maze test (Locomotor activity)

Y maze test (Working memory)

Y maze test (Spatial recognition memory)

C

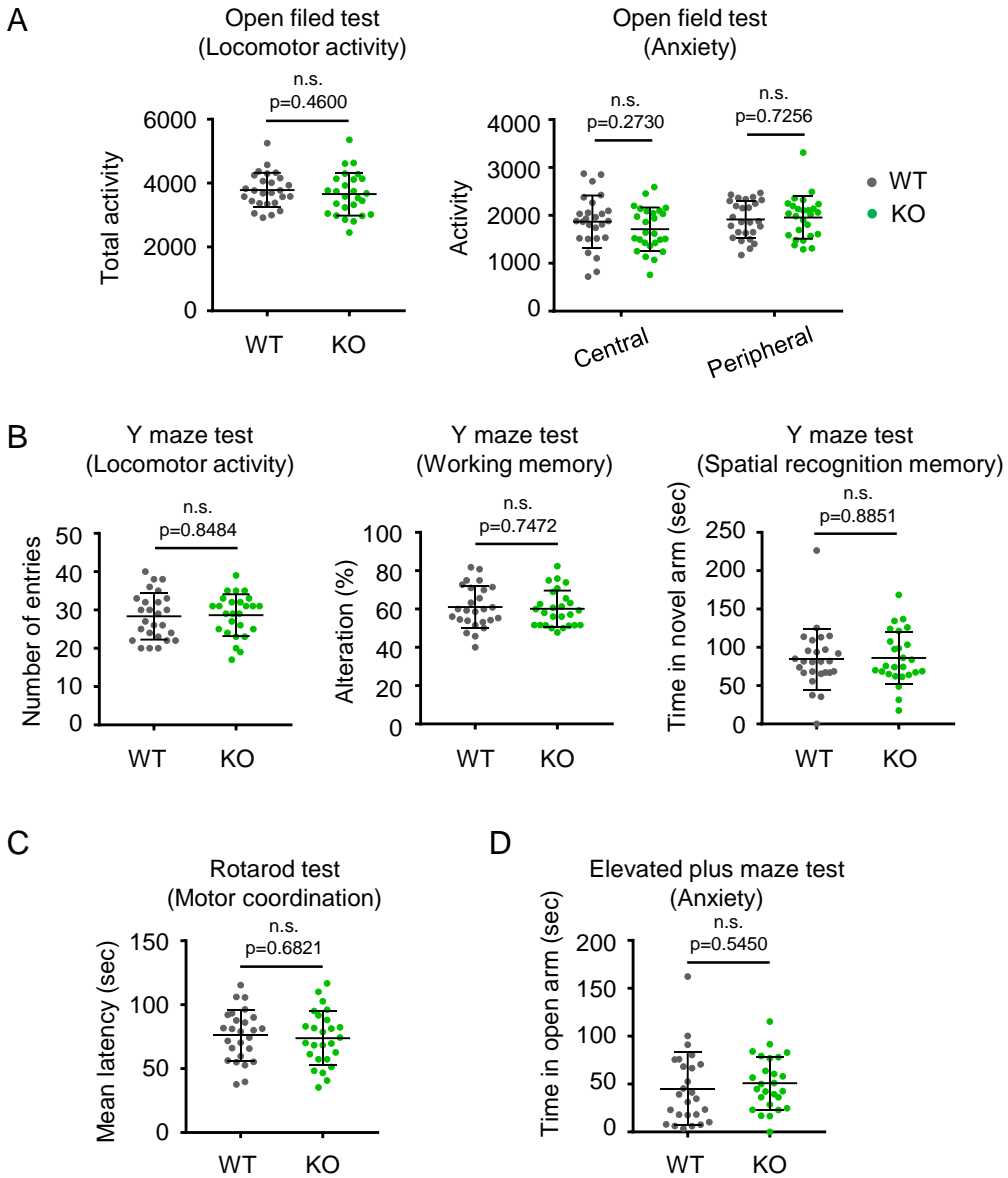**Rotarod test (Motor coordination)**

D

Elevated plus maze test (Anxiety)

Figure 4 — figure supplement 3. Itoh *et al.*